Stem Cell Reports
Article
ISSCR
OPEN ACCESS

*PSEN1*ΔE9, *APPswe*, and *APOE4* Confer Disparate Phenotypes in Human iPSC-Derived Microglia

Henna Konttinen,[1] Mauricio e Castro Cabral-da-Silva,[2] Sohvi Ohtonen,[1] Sara Wojciechowski,[1] Anastasia Shakirzyanova,[1] Simone Caligola,[3] Rosalba Giugno,[3] Yevheniia Ishchenko,[1] Damián Hernández,[4,5,6] Mohammad Feroze Fazaludeen,[1] Shaila Eamen,[1] Mireia Gómez Budia,[1] Ilkka Fagerlund,[1] Flavia Scoyni,[1] Paula Korhonen,[1] Nadine Huber,[1] Annakaisa Haapasalo,[1] Alex W. Hewitt,[4,5,7] James Vickers,[8] Grady C. Smith,[2] Minna Oksanen,[1] Caroline Graff,[9,10] Katja M. Kanninen,[1] Sarka Lehtonen,[1] Nicholas Propson,[11] Michael P. Schwartz,[12] Alice Pébay,[4,5,6] Jari Koistinaho,[1,13] Lezanne Ooi,[2] and Tarja Malm[1,*]

[1]A.I.Virtanen Institute for Molecular Sciences, University of Eastern Finland, Kuopio 70211, Finland
[2]School of Chemistry and Molecular Bioscience, Illawarra Health and Medical Research Institute, University of Wollongong, Wollongong, NSW 2522, Australia
[3]Department of Computer Science, University of Verona, Verona 37134, Italy
[4]Centre for Eye Research Australia, Royal Victorian Eye and Ear Hospital, Melbourne, VIC 3002, Australia
[5]Department of Surgery, the University of Melbourne, Melbourne, VIC 3002, Australia
[6]Department of Anatomy and Neuroscience, the University of Melbourne, Melbourne, VIC 3002, Australia
[7]School of Medicine, Menzies Institute for Medical Research, University of Tasmania, Hobart, VIC 7005, Australia
[8]Wicking Dementia Research and Education Centre, University of Tasmania, Hobart, TAS 7000, Australia
[9]Department NVS, Division of Neurogeriatrics, Karolinka Institutet, Stockholm 17176, Sweden
[10]Theme Aging, Genetics Unit, Karolinska University Hospital-Solna, Stockholm 17176, Sweden
[11]Department of Molecular and Cell Biology and the Huffington Center on Aging, Baylor College of Medicine, Houston, TX 77030, USA
[12]Department of Chemistry, University of Wisconsin-Madison, Madison, WI 53706, USA
[13]Neuroscience Center, University of Helsinki, Helsinki 00014, Finland
*Correspondence: tarja.malm@uef.fi
https://doi.org/10.1016/j.stemcr.2019.08.004

SUMMARY

Here we elucidate the effect of Alzheimer disease (AD)-predisposing genetic backgrounds, *APOE4*, *PSEN1ΔE9*, and *APPswe*, on functionality of human microglia-like cells (iMGLs). We present a physiologically relevant high-yield protocol for producing iMGLs from induced pluripotent stem cells. Differentiation is directed with small molecules through primitive erythromyeloid progenitors to re-create microglial ontogeny from yolk sac. The iMGLs express microglial signature genes and respond to ADP with intracellular Ca^{2+} release distinguishing them from macrophages. Using 16 iPSC lines from healthy donors, AD patients and isogenic controls, we reveal that the *APOE4* genotype has a profound impact on several aspects of microglial functionality, whereas *PSEN1ΔE9* and *APPswe* mutations trigger minor alterations. The *APOE4* genotype impairs phagocytosis, migration, and metabolic activity of iMGLs but exacerbates their cytokine secretion. This indicates that *APOE4* iMGLs are fundamentally unable to mount normal microglial functionality in AD.

INTRODUCTION

Alzheimer disease (AD) is a progressive neurodegenerative disorder and the most common cause of dementia (Weuve et al., 2014). AD pathology begins decades before the onset of clinical symptoms and neuroinflammation is strongly indicated in its progression (Shi and Holtzman, 2018). Neuroinflammation is mediated by microglia, the innate immune cells of the CNS. Microglia originate from erythromyeloid progenitor cells (EMPs) in the embryonic yolk sac (Ginhoux et al., 2013) and play pivotal roles in CNS development, as well as in tissue maintenance, injury response, and pathogen defense (Colonna and Butovsky, 2017). In AD, microglia are aberrantly activated and their normal functions are compromised (Saijo and Glass, 2011).

The major genetic risk factor for multifactorial late-onset AD (LOAD) (Liu et al., 2013) is a gene variant apolipoprotein E4 (*APOE4*), whereas inherited genetic mutations in presenilin 1 (*PSEN1*), presenilin 2 (*PSEN2*), or amyloid precursor protein (*APP*) genes (Selkoe, 1998) cause rarer early-onset familial AD (FAD) (Bagyinszky et al., 2014). Human *APOE* is primarily expressed in three variants, the most abundant *APOE3* being neutral, and the rarest *APOE2* being protective in AD. All forms are involved in transport and elimination of lipids, but a common mode of action in the brain remains largely unexplored. *APOE* is highly expressed in microglia, and *APOE4* is shown to promote the neurodegeneration-associated inflammatory phenotype of mouse microglia (Krasemann et al., 2017) and alter functions of human microglia-like cells (iMGLs) (Lin et al., 2018). However, the precise role of *APOE4* in the development of AD remains elusive. *PSEN1* and *APP* participate in the production of neurotoxic amyloid-beta (Aβ) peptide, the main component of the amyloid plaques found in the brains of AD patients. The expression of *APP* and *PSEN1* in microglia is shown to increase upon brain insults (Banati

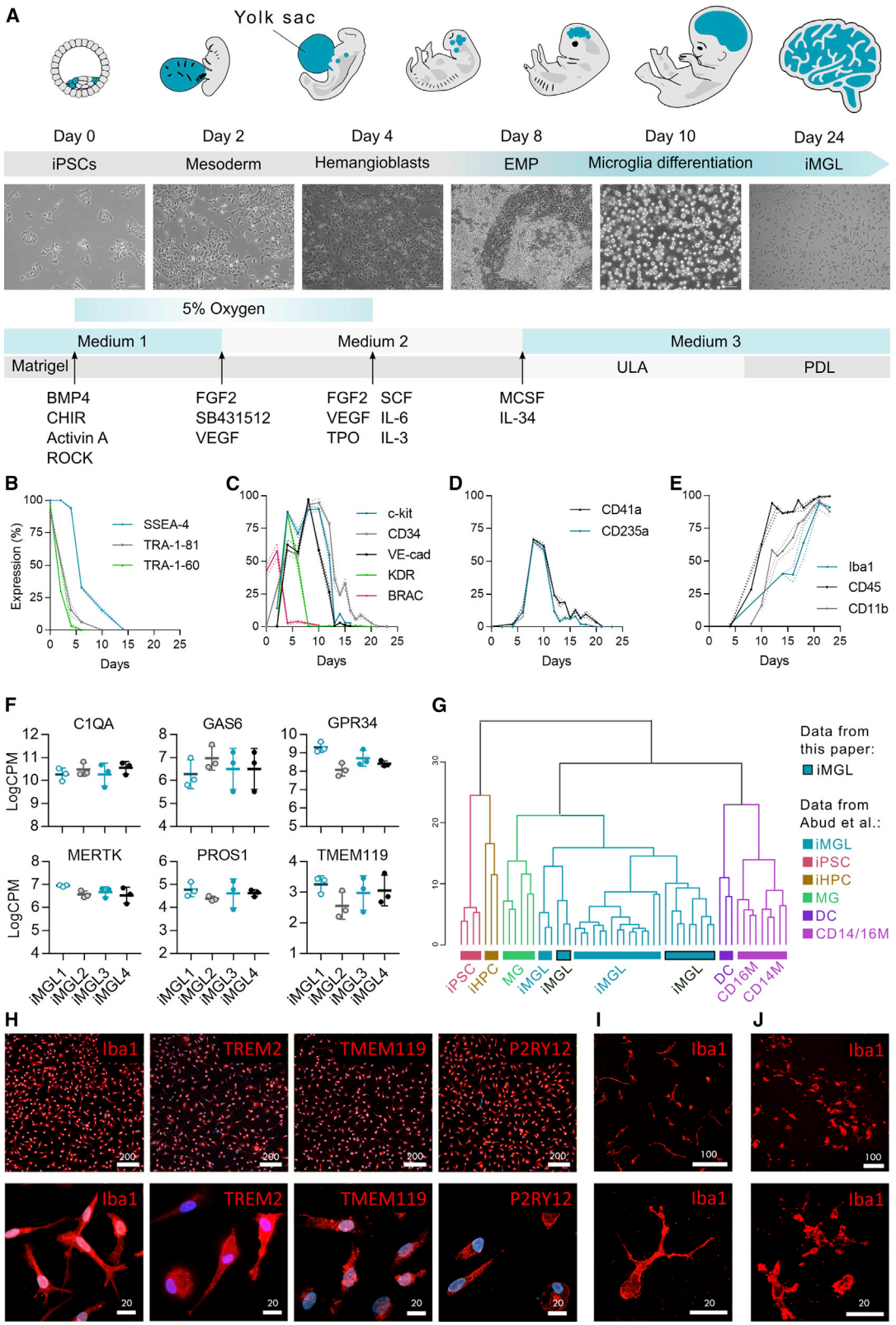

(legend on next page)

et al., 1993; Nadler et al., 2008) and these genes are implicated in inflammatory processes (Manocha et al., 2016; Zhao et al., 2017), but it is unclear whether they contribute to AD through microglial functions.

Given the central role of microglia in AD and the lack of knowledge of FAD mutations or *APOE4* in human microglia, we established a method to generate iMGLs from induced pluripotent stem cells (iPSCs) carrying *APOE4* genotype or *PSEN1ΔE9* or *APPswe* mutations. iMGLs have a robust microglial phenotype and resemble recently published iPSC-derived microglia (Abud et al., 2017; Douvaras et al., 2017; McQuade et al., 2018). We conclude that *APOE4* genotype has a substantial impact on the function of iMGLs, whereas the FAD mutations have only minor effects. *APOE4* contributes particularly to reduced migration, increased proinflammatory responses and defective glycolytic and mitochondrial metabolism. This study elucidates the role of human microglia in disease pathogenesis in FAD and LOAD.

RESULTS

iPSCs Differentiate into iMGLs through Primitive Hematopoiesis

We developed a high-yield 24-day protocol to differentiate human iPSCs into iMGLs. To recapitulate microglial ontogeny from the yolk sac (Ginhoux et al., 2010; Kierdorf et al., 2013; Schwartz et al., 2015; Uenishi et al., 2014), we used small molecules under defined oxygen conditions to direct differentiation through primitive EMPs followed by microglial maturation (Figure 1A). Morphological changes and the expression of the key markers for each stage of differentiation were assessed by flow cytometry and phase-contrast microscopy (Figures 1B–1E and S1).

During the first differentiation days (D0–2), mesodermal lineage was induced with BMP4, Activin A and CHIR99021 under low oxygen (5% O_2) conditions and was accompanied with a reduction of pluripotency markers (Figure 1B). When the expression of mesodermal brachyury was the highest, 48 h after initiation (Figure 1C), basic fibroblast growth factor (bFGF), SB431542, vascular endothelial growth factor (VEGF), and insulin were applied to evoke hemogenic differentiation. Subsequently, the areas of endothelial-like cells formed (Figure S1) and the expression of hemogenic EMP markers KDR, CD117 (c-kit), VE-cadherin, and CD34 increased (Figure 1C). On D6–7, loosely attached round cells appeared with a high expression of primitive EMP markers CD235a (Sturgeon et al., 2014) and CD41a (Kennedy et al., 2007) (Figure 1D). MCSF1 and interleukin-34 (IL-34) were used to induce microglial differentiation and expansion on ultra-low attachment (ULA) dishes. On maturation, the expression of myeloid markers increased and on D24, 88% of cells expressed CD11b, 99% CD45, and 91% IBA1 when cultured on ULA dishes (Figure 1E). To mature iMGLs for functional experiments, D16 progenitors were cultured on poly-D-lysine (PDL)-coated vessels until D24 to promote ramified and elongated morphology and IBA1 expression (Figure S1).

The microglial identity of iMGLs was confirmed with whole-transcriptome analysis and qRT-PCR (Figures 1F and S2; Table S1). The microglial signature genes, *C1QA*, *GAS6*, *GPR34*, *MERTK*, *PROS1*, and *TMEM119* (Butovsky et al., 2014), were highly expressed (logCPM>2, Figures 1F and S2). Comparison of RNA sequencing profiles to published dataset GSE89189 (Abud et al., 2017) using microglia genes (Lavin et al., 2014) revealed that iMGLs cluster with published iPSC-derived microglia (Abud et al., 2017), as well as with human microglia (Zhang et al., 2014), but remain distinct from iPSCs and other tissue myeloid cells (Figures 1G and S2). Immunostaining of D24 iMGLs verified ubiquitous expression of IBA1, CX3CR1, and PU.1 (Figures 1H and S1) and, importantly, microglia-specific proteins TMEM119, P2RY12, and TREM2 (Bennett et al., 2016) (Figure 1H). Furthermore, iMGLs spontaneously migrated into 3D co-cultures and adopted a ramified morphology (Figures 1I and 1J). Thus, the iMGLs generated through induction of primitive EMPs show a typical microglia-like genetic signature and protein expression.

iMGLs Express *APP* and *PSEN1*, and *PSEN1*ΔE9 Mutation Leads to Expected Alterations in PSEN1 Endoproteolysis

To assess the reproducibility of the differentiation protocol, we successfully generated iMGLs from 16 different iPSC

Figure 1. iPSCs Differentiate into iMGLs through Primitive Hematopoiesis

(A–E) Schematic protocol (A). Percentages of positive cells analyzed by flow cytometry for markers of (B) pluripotency, (C) EMPs and mesodermal brachyury (BRAC), (D) primitive EMPs, and (E) and mature microglia. n = 4 cell lines, repeated in 3 batches.

(F) The expression of microglial signature genes in RNA sequencing (RNA-seq) data of D24 iMGLs as log2 CPM values. n = 3 batches, 4 cell lines.

(G) Hierarchical clustering of RNA-seq data shows that our iMGLs cluster with published iMGLs and human microglia (MG), but are distinct from dendritic cells (DCs), monocytes (CD14M and CD16M), iPSCs, and hematopoietic progenitor cells (HPCs) (Abud et al., 2017).

(H–J) Immunostainings of D24 iMGLs (H). Repeated with two batches for all cell lines. Images of iMGLs labeled with IBA1 (red) in (I) 3D-Matrigel co-culture with neurons and in (J) cerebral brain organoids. Repeated with two batches for 2–4 cell lines. Scale bars as μm. Data presented mean ± SEM.

See also Figures S1 and S2; Tables S1 and S2.

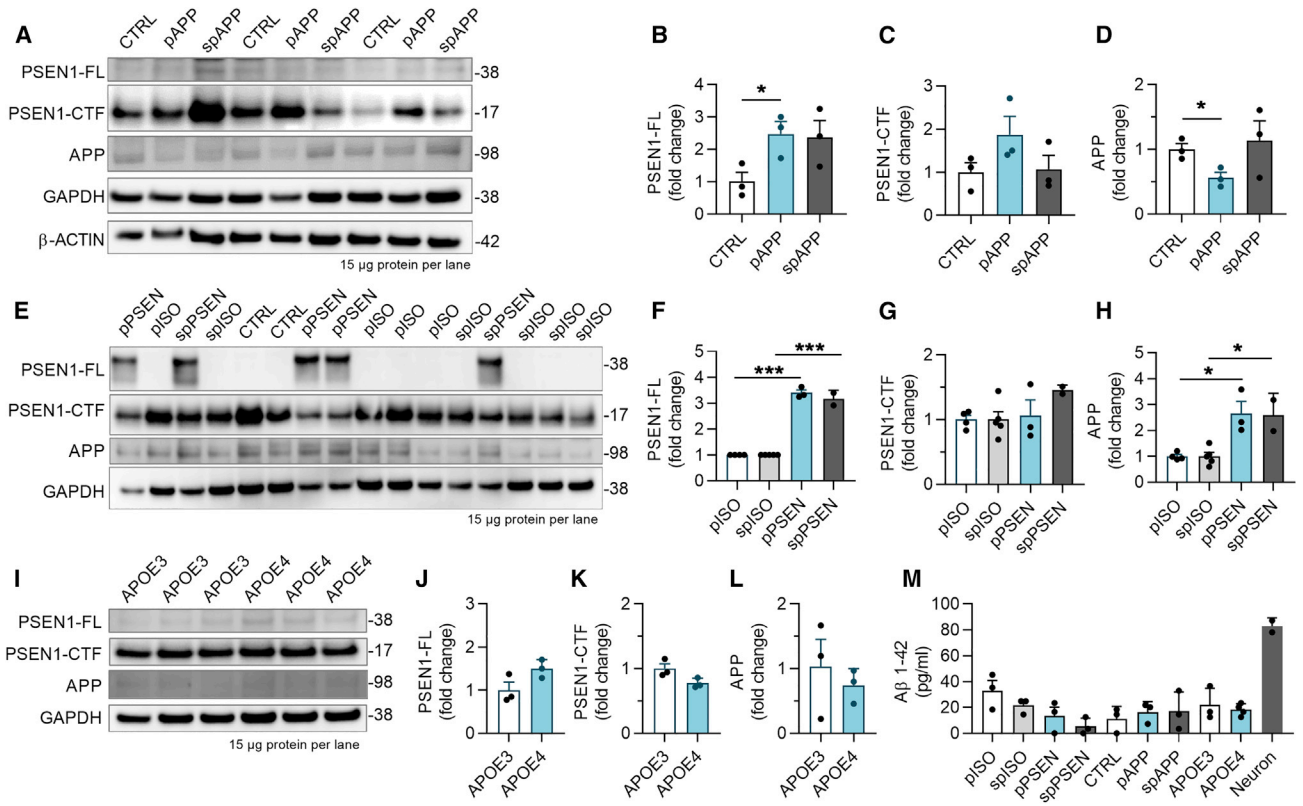

Figure 2. iMGLs Express APP and PSEN1 Proteins, and *PSEN1*ΔE9 Mutation Leads to Expected Alterations in PSEN1 Endoproteolysis

(A–L) Western blots for full-length (FL) and C-terminal fragment (CTF) of PSEN1 and APP proteins from 3 batches of control (CTRL) and *APPswe* (pAPP, spAPP) iMGLs (A). GAPDH and b-ACTIN as loading controls. Quantification of blots normalized to GAPDH for (B) PSEN1-FL, (C) PSEN1-CTF, and (D) APP protein. n = 3 batches. Respective western blots (E) and quantification (F–H) for *PSEN1ΔE9* iMGLs (pPSEN, spPSEN) and their isogenic controls (pISO and spISO). n = 2–5 batches. Western blots (I) for *APOE3* and *APOE4* iMGLs and quantification (J–L) for the proteins. n = 3 batches.

(M) Aβ 1-42 levels in cell culture medium after 48 h analyzed by ELISA. n = 2–5 batches for *APP* and *PSEN*; n = 3 wells for *APOE* repeated in three batches.

Data presented mean ± SEM unpaired two-tailed t test,*p < 0.05, **p < 0.01, ***p < 0.001. p, presymptomatic; sp, symptomatic. See also Figure S3.

lines (Table S3) with a 20-fold average yield. iPSCs originated from adult donors. Neutral *APOEε3/3* alleles (*APOE3*) were carried by five healthy subjects, two subjects with familial *KM670/*671NL Swedish double mutation in *APP* (*APPswe*) (Mullan et al., 1992), and two with a familial 4.6-kb deletion of exon 9 in *PSEN1* (*PSEN1*ΔE9) (Crook et al., 1998). Three subjects carried *APOEε4/4* alleles (*APOE4*) (Balez et al., 2016; Engel et al., 2018; Munoz et al., 2018; Ooi et al., 2013). One *APPswe* carrier had symptomatic AD (referred spAPP) and one was presymptomatic (pAPP) with no clinical diagnosis. Similarly, one *PSEN1ΔE9* carrier was presymptomatic (pPSEN) and one had AD diagnosis (spPSEN). The effect of *PSEN1ΔE9* mutation was validated with gene-corrected isogenic control lines from the symptomatic (spISO) and the presymptomatic (pISO) *PSEN1*ΔE9 carriers (Oksanen et al., 2017). Pluripotency and the karyotype of previously unpublished pAPP, *APOE3*, and *APOE4* lines were characterized (Figure S3).

We next analyzed the effect of genetic background on processing of APP protein into toxic Aβ. *APPswe* iMGLs showed 2.5-fold increase in PSEN1 protein but no consistent changes in APP compared with control cells (Figures 2A–2D). As expected, *PSEN1*ΔE9 iMGLs showed a robust accumulation of PSEN1 and a 3-fold increase in APP compared with isogenic controls (Figures 2E–2H), thereby establishing that the *PSEN1*ΔE9 mutation resulted in a loss of γ-secretase cleavage of APP. Furthermore, *APOE3* and *APOE4* lines showed low levels of APP, PSEN1, and C-terminal fragments of PSEN1, and no differences between the genotypes (Figures 2I–2L). Quantification of Aβ fragments from cell lysates and culture media revealed that iMGLs had no intracellular Aβ and secreted only

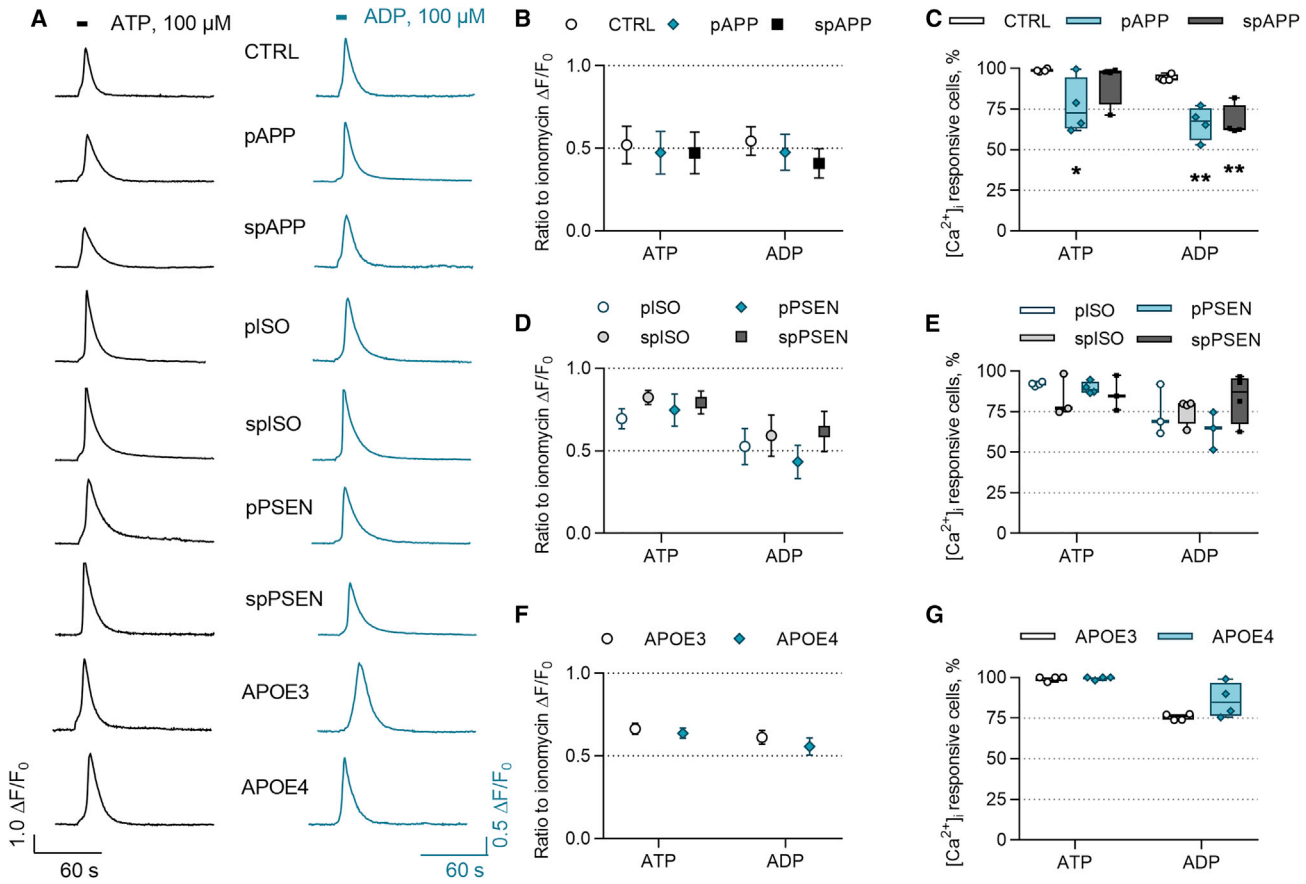

Figure 3. ATP and ADP Evoke Intracellular Calcium $[Ca^{2+}]_i$ Transients in iMGLs

(A) Example traces of $[Ca^{2+}]_i$ transients following 100 μM ATP (left panel) and ADP (right panel) applications for 5 s (indicated by bars) in iMGLs loaded with the Ca^{2+} indicator Fluo-4 AM.

(B) The ratio of maximum amplitudes normalized to amplitudes evoked by ionomycin that was applied in the end of experiment and used as inclusion criteria. n = 4 batches, each with 9–10 coverslips, altogether 3,994 CTRL, 3,015 pAPP, and 3,906 spAPP cells.

(C–E) Percentages of ATP- and ADP-responsive cells in *APPswe* lines compared with control iMGLs (C). Ratio of maximum amplitudes (D) and percentages of responsive cells (E) obtained from isogenic and *PSENΔE9* iMGLs. n = 4 batches, each with 9–12 coverslips, altogether 1,969 pISO, 2,355 spISO, 1,856 pPSEN, and 2,823 spPSEN cells.

(F and G) Similar data for *APOE3* and *APOE4* iMGLs. n = 4 coverslips, altogether 482 *APOE3* and 991 *APOE4* cells, repeated in three batches. Data presented mean ± SEM unpaired two-tailed t test or one-way ANOVA followed by Bonferroni's post hoc test, *p < 0.05, **p < 0.01. CTRL, control; p, presymptomatic; sp, symptomatic; PSEN, *PSEN1ΔE9*; APP, *APPswe*; and ISO, isogenic control iMGLs.

Aβ1-42 at similar levels regardless of the genotype (Figure 2M). Taken together, all cell lines had a normal karyotype and expressed FAD mutations or LOAD risk variants supporting their use for studying AD, even though genotypes failed to alter iMGL Aβ production.

ATP and ADP Evoke Intracellular Calcium Transients in iMGLs

Since calcium may control microglial functions under resting and activated conditions (Hoffmann et al., 2003), we next investigated intracellular calcium $[Ca^{2+}]_i$ transients in response to ATP and ADP. The representative traces of $[Ca^{2+}]_i$ transients demonstrate similar responses in all genotypes (Figure 3A). The average amplitudes of the responding cells were equal in control and *APPswe* iMGLs (Figure 3B). In contrast, there was a 22% reduction in ATP-responsive cells in pAPP iMGLs and a 27% reduction in ADP-responsive cells in both pre- and symptomatic *APPswe* iMGLs compared with control (Figure 3C). Equal amplitudes and percentages of responsive cells were observed for isogenic and *PSEN1*ΔE9 iMGLs (Figures 3D and 3E), and for *APOE3* and *APOE4* iMGLs (Figures 3F and 3G) demonstrating the consistent functionality of iMGLs harboring these genotypes. Collectively, all cell lines responded to ADP and ATP by intracellular calcium release, supporting microglia-like functionality of the

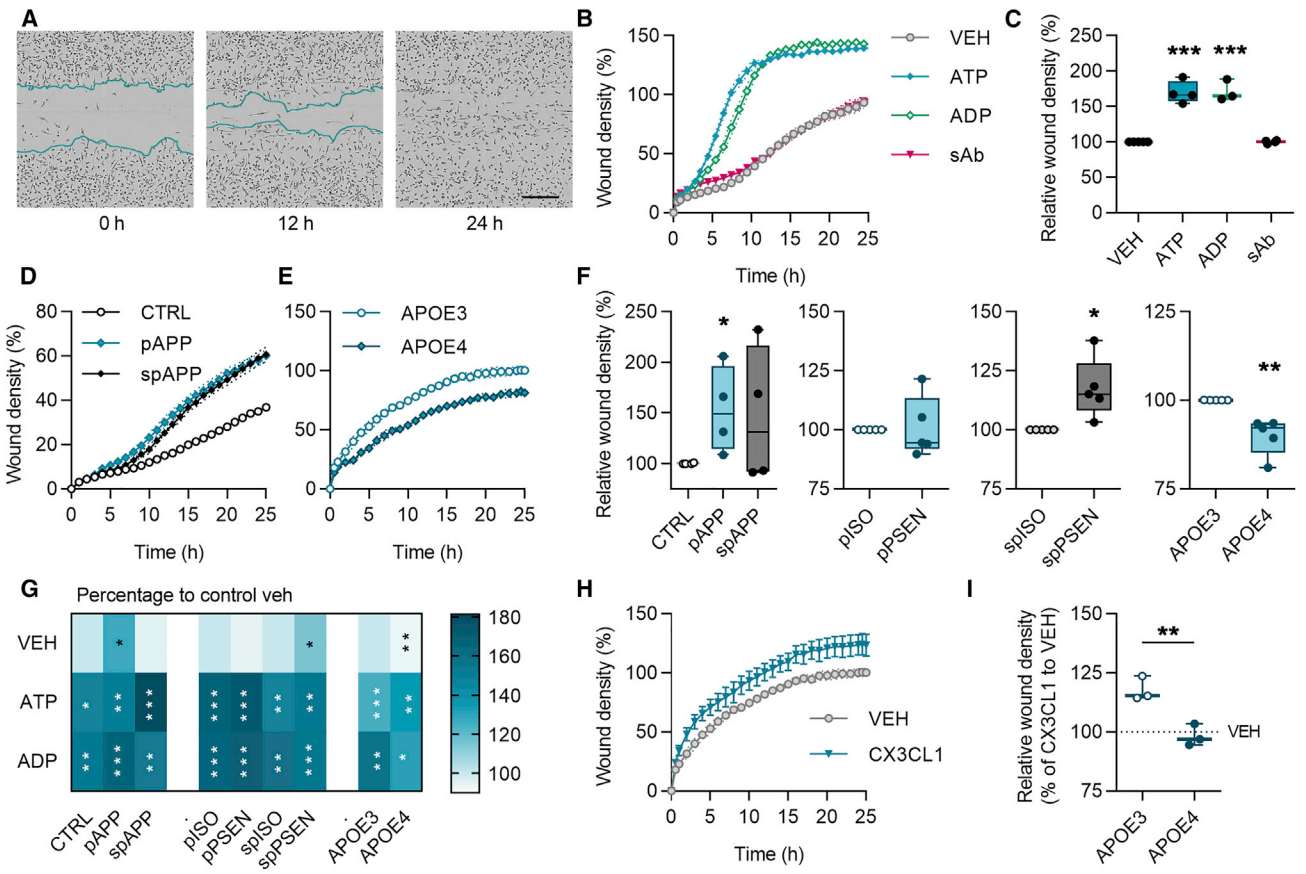

Figure 4. Chemokinesis Is Accelerated in *APPswe* and *PSEN1ΔE9* iMGLs but Decelerated in *APOE4* iMGLs

(A) Representative images of iMGLs in scratch wound migration assay at 0, 12, and 24 h time points. Scale bar 300 μm.

(B) Wound densities measured for 25 h with vehicle (VEH), 100 μM ATP, 100 μM ADP, or 1-μM soluble sAβ treatments.

(C–E) Wound densities at 24 h normalized to vehicle (C). Time curves for (D) control (CTRL) and *APPswe* (APP), and (E) *APOE3* and *APOE4* iMGLs.

(F) Wound densities at 24 h normalized to control or isogenic (ISO) iMGLs.

(G) A heatmap for increase (darker color) or decrease (lighter color) in wound density compared with vehicle. White asterisks indicate significance compared with vehicle and black asterisks to control genotype.

(H) Time curves for wound density with 100 μM fractalkine (CX3CL1) treatment in *APO3* iMGLs.

(I) Corresponding wound density at 24 h normalized to vehicle for *APOE* iMGLs. Curve graphs show a representative experiment of three replicates, n = 3–5 wells. Boxplots and heatmap show normalized results from n = 3–5 replicate batches.

Data presented mean ± SEM, unpaired two-tailed t test, *p < 0.05, *p < 0.01, ***p < 0.001. p, presymptomatic; sp, symptomatic. See also Figure S4.

iMGLs. Reduction in *APPswe* responses suggests that FAD mutation can alter intracellular calcium signaling.

Chemokinesis Is Accelerated in *APPswe* and *PSEN1ΔE9* iMGLs but Decelerated in *APOE4* iMGLs

Microglial migration to the injury site is crucial for maintaining homeostasis in the brain. We analyzed the chemokinesis of iMGLs using a scratch wound assay with live-cell imaging for 24 h (Figure 4A). Acute application of ATP and ADP, which can be released from injured neurons, increased migration in all tested cell lines, whereas soluble oligomeric Aβ (sAβ) failed to alter migration (Figures 4B, 4C, and S4). We observed increased basal migration in *APPswe* lines compared with control iMGLs as well as in spPSEN iMGLs compared with their isogenic controls (Figures 4D, 4F, and S4). In contrast, *APOE4* genotype reduced basal migration (Figures 4E and 4F). ATP or ADP induced similar increase in migration in all genotypes (Figure 4G). In contrast, migration evoked by fractalkine was restrained in *APOE4* iMGLs compared with *APOE3* (Figures 4H and 4I), indicating impairment in motility in response to this neuron-derived chemokine. The migration was reduced if fetal bovine serum (FBS) was withdrawn from cell culture and therefore the experiments were performed in the

presence of FBS (Figure 4S). Overall, all iMGL lines migrated and responded to different stimuli as expected for microglia. A reduction in *APOE4* and a mild increase in APP and PSEN1 iMGLs suggest that LOAD risk variant and FAD mutations have different effects on microglial functions.

Phagocytosis Is Dampened in *APOE4* iMGLs, but Not in *APPswe* or *PSEN1ΔE9* iMGLs

Since microglia fail to efficiently clear Aβ plaques in AD (Lee and Landreth, 2010), we examined phagocytosis by live-cell imaging. iMGLs spontaneously phagocytosed pHrodo Zymosan A bioparticles (Figures 5A and 5B) equivalently despite of their genotypes (Figures 5C, 5D, and S4). Since *APOE4* variant was recently reported to reduce phagocytosis in iPSC-derived microglia (Lin et al., 2018), we investigated *APOE* iMGLs also with confocal microscopy and with fewer number of larger fluorescein isothiocyanate (FITC) Zymosan A bioparticles to count internalized particles (Figures 5E and 5F). Indeed, despite the equal overall intensity of phagocytosed pHrodo particles (Figure 5G), *APOE4* iMGLs ingested a smaller number of FITC particles per cell compared with *APOE3* (Figure 5H).

Next, we tested whether proinflammatory stimuli attenuate the phagocytosis of iMGLs as reported for murine microglia (Koenigsknecht-Talboo and Landreth, 2005). iMGLs were pretreated with lipopolysaccharide (LPS), interferon γ (IFN-γ), or both LPS and IFN-γ (LPS-IFN-γ) for 24 h or treated with sAβ or insoluble fibrillary (fAβ) Aβ1-42 at the time of particle application. Unexpectedly, LPS failed to alter phagocytosis of pHrodo beads, whereas IFN-γ or LPS-IFN-γ suppressed it (Figures 5I–5L). Withdrawal of stimuli before to the measurement did not restore IFN-γ-mediated suppression, but in the LPS-pretreated group phagocytosis was first abrogated and then potentiated 5 h after withdrawal (Figure S4). Addition of fAβ only slightly enhanced the phagocytosis of pHrodo beads in presymptomatic isogenic and *PSEN1ΔE9* iMGLs, whereas sAβ had no effect (Figures 5J and 5K).

iMGLs phagocytosed also fluorescent Aβ1-42 spontaneously (Figure 5M). *APPswe* iMGLs internalized 1.2-fold more Aβ compared with their controls (Figures 5N and 5O). *PSEN1ΔE9* or *APOE4* genotypes had no effect (Figure S4). To test the impact of proinflammatory activation on Aβ phagocytosis, we treated the cells with LPS, sAβ, or fAβ simultaneously with fluorescent Aβ. LPS reduced Aβ phagocytosis only in isogenic and *PSEN1ΔE9* iMGLs (Figure S4), and fAβ induced engorged vacuoles in all genotypes (Figure 5P). In summary, iMGLs presented microglia-like phagocytosis of both particles and Aβ and altered phagocytosis upon inflammatory stimuli. Only *APOE4* iMGLs showed mild impairment in phagocytosis.

Cytokine Release under Proinflammatory Conditions Is Aggravated in *APOE4* iMGLs but Decreased in *PSEN1*ΔE9 and *APPswe* iMGLs

To study cytokine release, conditioned medium was analyzed with cytokine bead array after 24 h treatment with vehicle, LPS, IFN-γ, or LPS-IFN-γ (Figure 6A). Under basal conditions, the levels of proinflammatory cytokines IL-6, tumor necrosis factor alpha (TNF-α), regulated on activation, normal T cell expressed and secreted (RANTES), and granulocyte-macrophage colony-stimulating factor (GM-CSF) were negligible (<1 pg/mL), whereas IL-8 levels were small (10 pg/mL) and MCP1 reached even 1 ng/mL concentrations (Figure 6A). As expected, iMGLs robustly responded to LPS with significant induction in all measured cytokines. The combination of LPS-IFN-γ triggered similar or even higher release of cytokines except GM-CSF, whereas IFN-γ alone induced only small, yet detectable, increase.

We investigated further LPS-IFN-γ effect since it simulates *in vivo* damage-associated molecular patterns acting on Toll-like receptors and IFN-γ produced by CNS cells (Pulido-Salgado et al., 2018). *APPswe* iMGLs produced less TNF-α and MCP1 in response to LPS-IFN-γ compared with control iMGLs (Figure 6B). Similarly, *PSEN1ΔE9* iMGLs secreted less IL-6, TNF-α, and RANTES compared with their isogenic controls (Figure 6C). Concomitantly, LPS or IFN-γ alone resulted in decreased cytokine secretion in iMGLs harboring these genotypes (Figure S4). In contrast, *APOE4* iMGLs produced more cytokines compared with *APOE3* iMGLs upon treatment with LPS-IFN-γ (Figure 6D), LPS or IFN-γ (Figure S4). Taken together, *APOE4* genotype increased cytokine secretion, whereas FAD mutations reduced it.

Metabolism of iMGLs Is Altered under Pro- and Anti-inflammatory Stimuli and by *APOE4* Genetic Background

To investigate metabolism under anti- or proinflammatory stimuli we measured the cellular respiration of iMGLs after 24 h treatment with IL-4, LPS, IFN-γ, or LPS-IFN-γ (Figures 7A and 7B). An anti-inflammatory IL-4 increased parameters of oxidative respiration, whereas proinflammatory LPS and LPS-IFN-γ reduced them (Figure 7C). IFN-γ increased all parameters except ATP production (Figure 7C). Compared with LPS, LPS-IFN-γ reversed oxidative parameters toward the levels of the vehicle (Figure 7C). On the contrary, all proinflammatory stimuli increased anaerobic glycolysis and glycolytic capacity indicating a shift from oxidative respiration toward anaerobic glycolysis (Figure 7D). The pooled data for LPS normalized to the vehicle confirmed the equal shifts in all genotypes, except the proton leak was increased in pAPP and glycolytic capacity in spAPP compared with control iMGLs (Figure 7E).

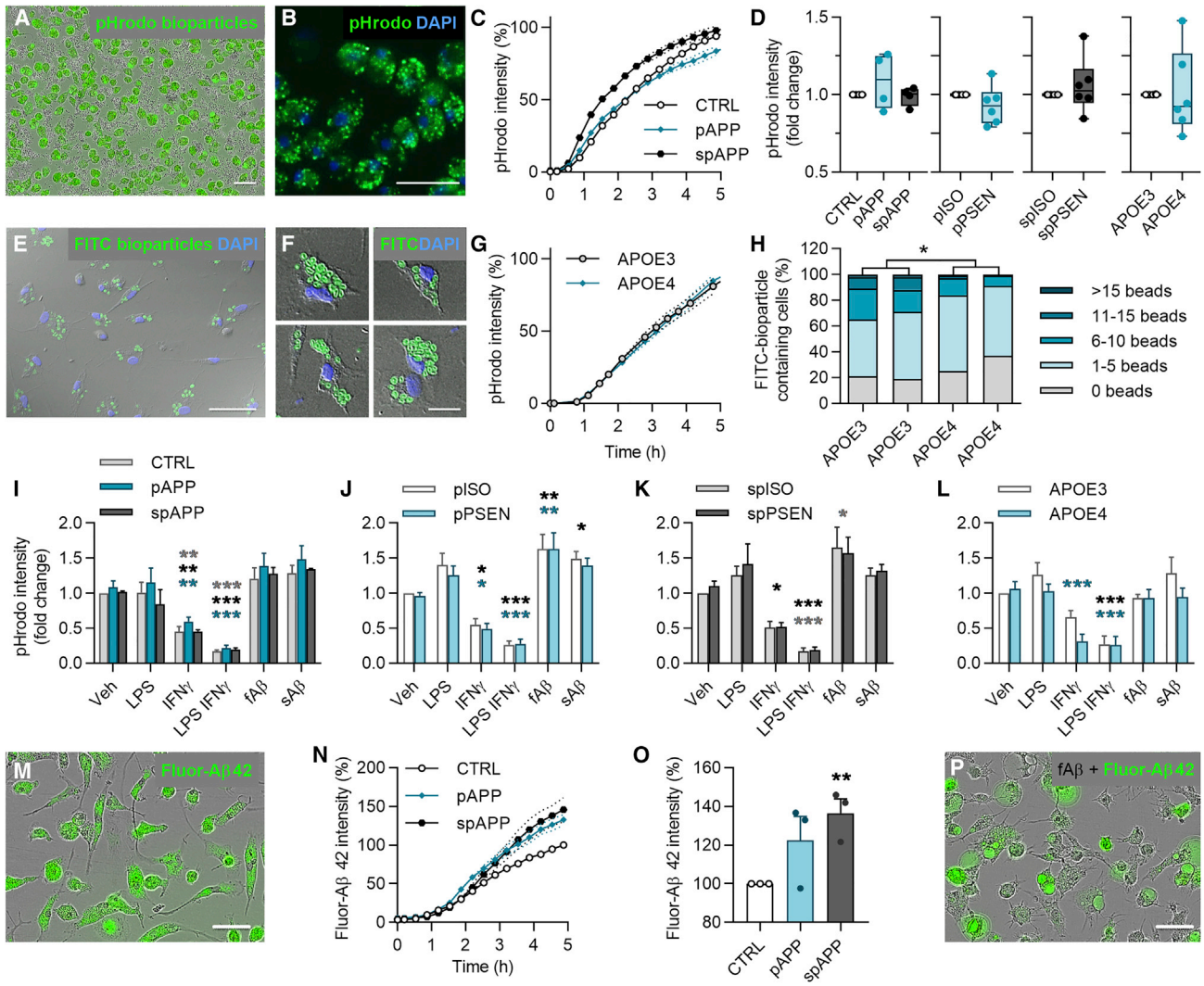

Figure 5. Phagocytosis Is Dampened in *APOE4* iMGLs, but not in *APPswe* or *PSEN1ΔE9* iMGLs

(A and B) Representative images of phagocytosed green pHrodo Zymosan A bioparticles in iMGLs at 5 h.

(C) Time curves for pHrodo fluorescence intensity in control (CTRL) and *APPswe* (APP) iMGLs normalized to cell amount.

(D) Respective boxplots at 5 h normalized to control or isogenic (ISO) iMGLs.

(E and F) Representative images of phagocytosed FITC Zymosan A bioparticles in iMGLs.

(G) pHrodo time curves for *APOE3* and *APOE4* iMGLs.

(H) Percentages of *APOE* iMGLs that internalized certain number of FITC particles per cell. n = 290–750 cells.

(I–L) pHrodo intensity at 5 h, after 24 h pretreatment with 100 ng/mL LPS, 20 ng/mL IFN-γ, or LPS-IFN-γ, or with simultaneous treatment with 0.5 μM soluble sAβ or fibrillar fAβ, compared with vehicle (Veh) in APPswe (I), pPSEN (J), spPSEN (K), and APOE (L) iMGLs.

(M) Representative image of phagocytosed green fluor-Aβ1-42 in iMGLs at 5 h.

(N) Time curves for fluorescence intensity of fluor-Aβ in control and *APPswe* iMGLs.

(O) Respective bar graphs at 5 h normalized to control iMGLs.

(P) Representative image of iMGLs treated with fluor-Aβ and fAβ depicting enlarged vacuoles. Scale bars, 50 μm. Curve graphs show a representative experiment of 3 replicates, n = 4 wells. Boxplots and bar graphs show normalized results from n = 2–6 replicate batches. Data presented mean ± SEM unpaired two-tailed t test or two-way ANOVA with Bonferroni's post hoc test,*p < 0.05, **p < 0.01, ***p < 0.001. p, presymptomatic; sp, symptomatic; PSEN, *PSEN1ΔE9* iMGLs. See also Figure S4.

To elucidate whether AD-predisposing genetic backgrounds provoked a metabolic shift toward a proinflammatory glycolytic phenotype, we next compared respiration between the genotypes without stimulus. FAD mutations did not alter the metabolism (Figures 7F and 7G). In contrast, oxygen consumption rate was lower in *APOE4*

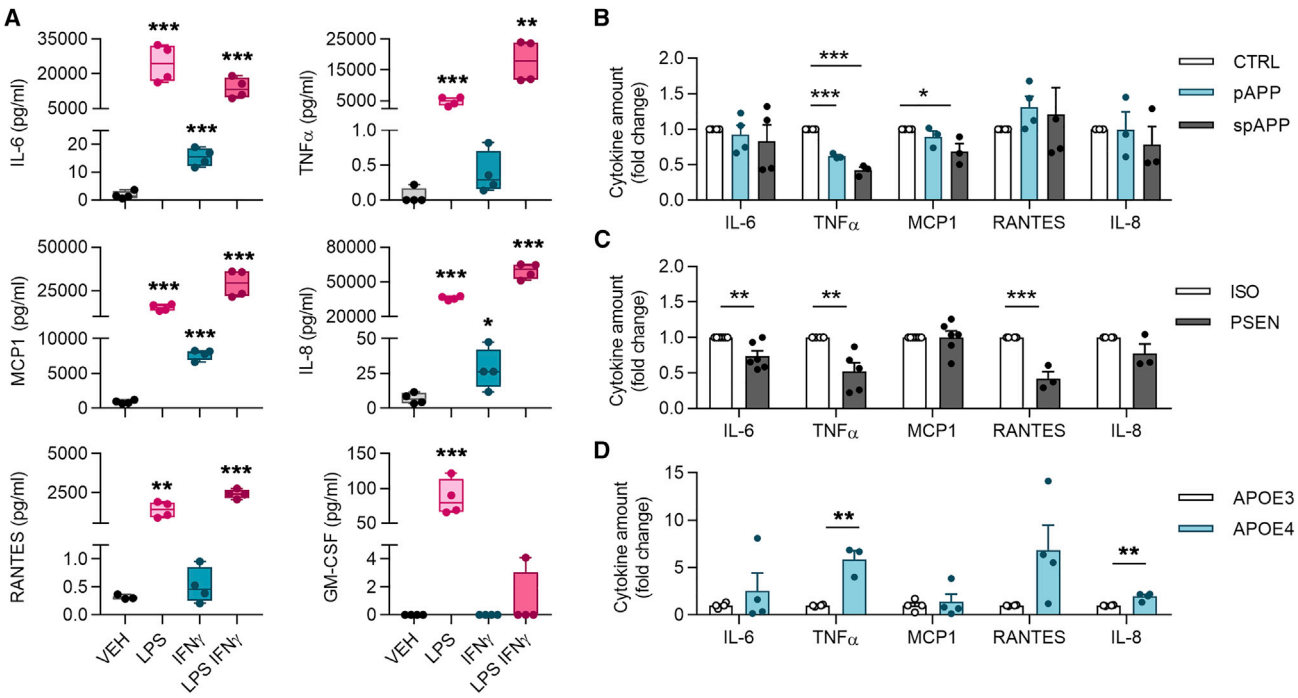

Figure 6. Cytokine Release under Proinflammatory Conditions Is Aggravated in *APOE4* iMGLs but Decreased in *PSEN1ΔE9* and *APPswe* iMGLs

(A) iMGLs secrete cytokines when stimulated for 24 h with LPS 100 ng/mL, IFN-γ 20 ng/mL, or their combination LPS-IFN-γ as measured from media by cytometric bead array assay. Representative graphs. n = 4 wells.

(B) spAPP iMGLs released less TNF-α, and pAPP less TNF-α and MCP1, compared with control iMGLs in response to LPS-IFN-γ treatment.

(C) *PSEN1*ΔE9 iMGLs released less IL-6, TNF-α, and RANTES compared with isogenic iMGLs.

(D) In contrast, *APOE4* iMGLs released aggregated amounts of TNF-α and IL-8 compared with *APOE3*. For (B–D) n = 3–6 batches, each with 4 wells.

Data presented mean ± SEM unpaired two-tailed t test, *p < 0.05, *p < 0.01, ***p < 0.001. See also Figure S4. CTRL, control; p, presymptomatic; sp, symptomatic; PSEN, *PSEN1ΔE9*; APP, *APPswe*; and ISO, isogenic control iMGLs.

iMGLs compared with *APOE3* iMGLs, demonstrating a similar shift as with LPS treatment (Figure 7H). Surprisingly, the *APOE4* genotype led to a reduced extracellular acidification (Figure 7H), whereas LPS had increased it (Figure 7A). In accordance, *APOE4* iMGLs showed a reduction in all mitochondrial parameters compared with the *APOE3* iMGLs (Figure 7I).

DISCUSSION

Here, we demonstrate the power of iPSC-derived microglia to elucidate distinct functional phenotypes of human microglia in disease. Differentiated iMGLs show a typical microglia-like gene and protein expression and respond to inflammatory stimuli robustly in multiple functional assays. We pinpoint specific phenotypes in iMGLs with three AD-predisposing genetic backgrounds, revealing that *APOE4* has a profound impact on several aspects of microglial functionality, whereas *APPswe* and *PSEN1ΔE9* have minor effects. The distinct phenotypes were observed without changes in amounts of Aβ, suggesting that Aβ burden associated with *PSEN1ΔE9*, *APPswe*, and *APOE4* is of neuronal and astrocytic origin (Oberstein et al., 2015; Scheuner et al., 1996), and that human microglia with these genotypes harbor alternative mechanisms underlying development and progression of AD.

This study reveals that *APOE4* iMGLs are fundamentally unable to mount normal microglial functionality as hypothesized for AD (Saijo and Glass, 2011). The *APOE4* genotype impaired phagocytosis and migration, and aggravated inflammatory responses of iMGLs, suggesting that *APOE4* confers iMGLs toward a proinflammatory disease-associated microglial (DAM) phenotype (Lin et al., 2018; Olah et al., 2018). We also reported similar responses to proinflammatory IFN-γ and LPS in phagocytosis and cytokine release, consistent with murine microglia (Townsend et al., 2005, Koenigsknecht-Talboo and Landreth, 2005). *APOE4* conferred decrease in migration at basal level and in response to fractalkine, although no changes in

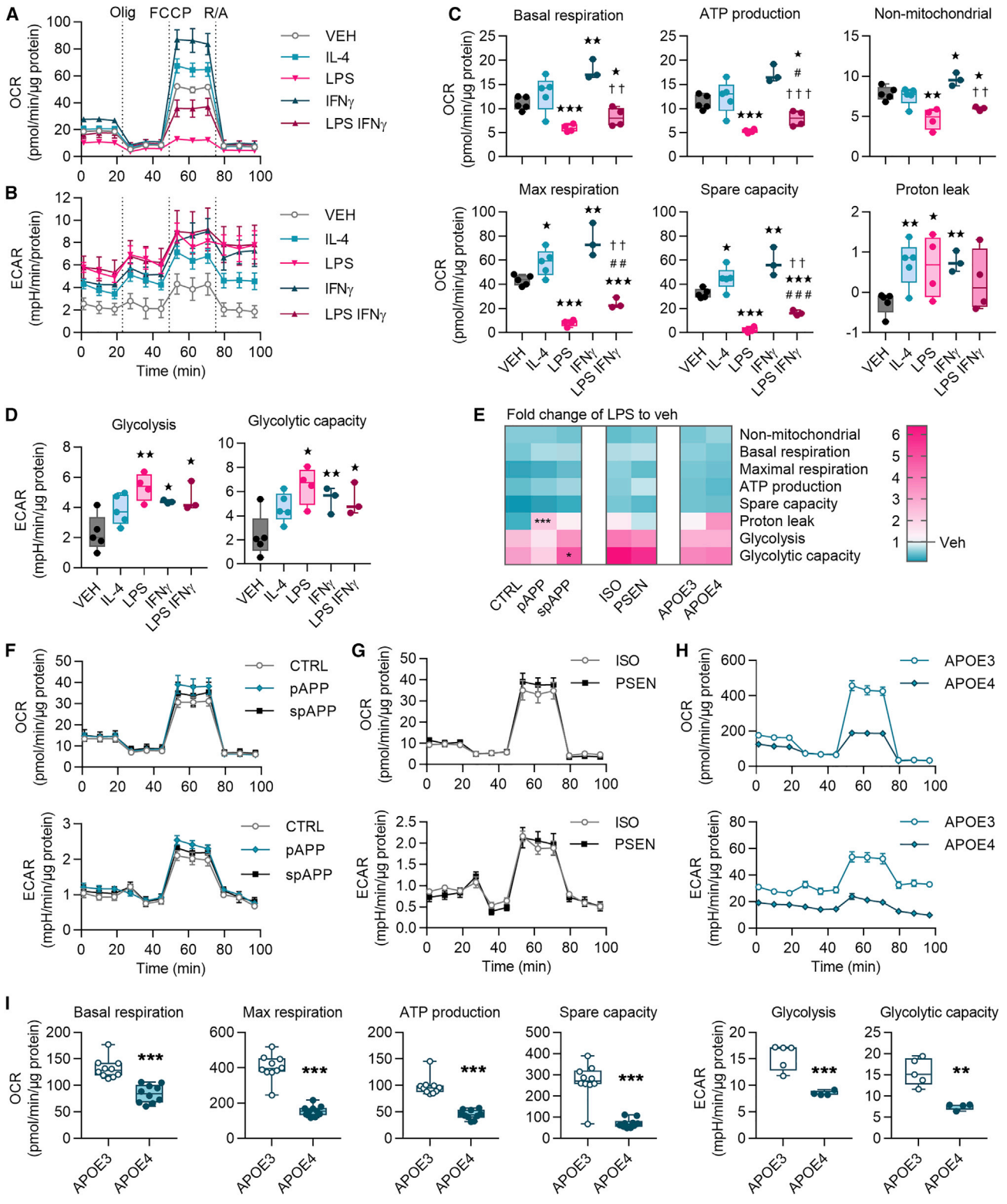

Figure 7. Metabolism of iMGLs Is Altered under Pro- and Anti-inflammatory Stimuli and by *APOE4* Genetic Background

(A) Representative oxygen consumption rate (OCR) curves for iMGLs following 24 h vehicle (VEH), LPS, IL-4, IFN-γ, and LPS-IFN-γ treatments, all 20 ng/mL. n = 3–5 wells.

(legend continued on next page)

P2RY12 or CX3CR1 expression were observed. Furthermore, no increase in chemokinesis upon Aβ exposure was seen in scratch wound assay, although invasion assays could be more relevant to study chemotaxis. In mouse models, the switch to DAM is triggered by TREM2-APOE interaction (Krasemann et al., 2017); however, exact mechanisms underlying human *APOE4*-induced inflammatory phenotype in AD microglia remain incompletely defined.

We extend these findings to highlight a novel role of *APOE4* in impaired metabolism of microglia. The cellular metabolism was robustly shifted in all iMGLs in response to inflammatory stimuli. LPS induced switch from oxidative metabolism to anaerobic glycolysis in line with recent evidence (Ghosh et al., 2018; Orihuela et al., 2016), whereas less studied IFN-γ increased both oxidative and glycolytic metabolism, supporting its role in the priming of microglia to meet the energy demands upon activation (Ta et al., 2019). Metabolic shift toward glycolysis is reported to occur also in AD microglia with *TREM2* mutations (Ulland et al., 2017). On the contrary, we observed a general downregulation of all metabolic parameters, both oxidative and glycolytic, in *APOE4* iMGLs. Thus, *APOE4*-induced inhibition of microglial metabolism and phagocytosis accompanied with heightened cytokine release may partly explain the development AD-related plaque burden in the brain.

In contrast to *APOE4*, the FAD mutations caused only a slight decrease in proinflammatory cytokine release and increase in chemokinesis. Unlike that recently reported for sporadic AD lines (Xu et al., 2019), *APPswe* and *PSEN1*ΔE9 mutations did not predispose iMGLs toward a more proinflammatory phenotype, but rather toward a senescent phenotype incapable of implementing a full inflammatory response. Cytokine-mediated inflammation has been strongly established in multiple animal models of AD, but human patients show varied results (Wang et al., 2015; Smith et al., 2012, Barroeta-Espar et al., 2019). *PSEN2* rather than *PSEN1* has been reported to modulate microglial cytokine release (Jayadev et al., 2013). iMGLs secreted similar levels of cytokines with human autopsy microglia (Rustenhoven et al., 2016), and decrease in FAD iMGLs is consistent with lower cytokine levels reported in certain brain areas of AD patients compared with non-AD subjects (Lanzrein et al., 1998). These mild and opposite outcomes in iMGLs with FAD mutations compared with the *APOE4* genotype indicate that functionality of human microglia with different genetic backgrounds is sensitively and distinctly modulated, and that pathogenic effects of *APPswe* and *PSEN1ΔE9* are mainly mediated by other cell types.

To elucidate the aforementioned functional AD phenotypes of human microglia we used a novel method to generate iMGLs. Several groups have recently reported protocols (Douvaras et al., 2017; Haenseler et al., 2017; Muffat et al., 2016; Pandya et al., 2017) to produce microglia from stem cells, and our protocol closely resembles methods from the Blurton-Jones group (Abud et al., 2017; McQuade et al., 2018). In our method, differentiation is initiated simply with a defined number of single cells to generate functional high-purity microglia-like cells in 24 days with a 20-fold yield. Importantly, we confirmed that most cells differentiate through primitive EMPs, the most critical step making microglia distinct from other tissue macrophages (Kennedy et al., 2007; Sturgeon et al., 2014). In our hands, low oxygen conditions during the early stages were pivotal in yielding considerable numbers of primitive EMPs, even though a recent study (McQuade et al., 2018) suggests that normoxic conditions would be advantageous for simplifying equipment. The microglia-like identity of iMGLs was confirmed with high expression of microglial signature genes and low expression of macrophage genes, since microglial genes are expressed to some extent also in primitive macrophages (Haenseler et al., 2017).

Considering that iPSC-models fundamentally produce rather immature cell types, the iMGLs probably represent relatively young microglia. In accordance, P2RY12, a marker for mature microglia, was expressed at a relatively low level (Bennett et al., 2016; Butovsky et al., 2014). iMGLs also exhibited a high migration capacity in response to chemotactic signals, such as ATP (De Simone et al., 2010; Lambert et al., 2010), as has been shown previously for young microglia (Caldeira et al., 2017). Thus, we recognize that the method can be further optimized by utilizing the advantages presented in other iPSC-derived microglia

(B–D) Corresponding extracellular acidification rate (ECAR) curves (B). Mitochondrial parameters calculated from (C) OCRs in (A and D) from ECARs in (B).

(E–H) Heatmap indicating decrease (blue) or increase (red) in fold change of mitochondrial parameters of LPS-treated iMGLs compared with vehicle (E). White equals 1. n = 5 CTRL, n = 4 pAPP, n = 2 spAPP, n = 3 *APOE3*, and n = 2 *APOE4* batches with 10 wells; n = 1 isogenic, and n = 3 *PSEN1* batches with 4–5 wells. Representative OCR and ECAR curves for (F) control and *APPswe*, (G) isogenic and *PSEN1*ΔE9, and for (H) *APOE4* and *APOE3* iMGLs. n = 5–10 wells, repeated with three batches.

(I) Mitochondrial parameters calculated from OCRs and ECARs in (H) *p < 0.05, **p < 0.01, ***p < 0.001 compared with vehicle, #compared with LPS, †compared with IFN-γ, two-tailed unpaired t test. Olig, oligomycin; FCCP, carbonyl cyanide-4-(trifluoromethoxy) phenylhydrazone; R/A, rotenone and antimycin A, each 1 μM. CTRL, control; p, presymptomatic; sp, symptomatic; PSEN, *PSEN1ΔE9*; APP, *APPswe*; and ISO, isogenic control iMGLs.

protocols. FBS could be replaced with more defined supplements to reduce potential unwanted priming that might mask subtle genotype differences and additional maturation factors, such as transforming growth factor β, CD200, and CX3CL1, could be applied.

Taken together, we report here a short and relatively easy to use protocol to differentiate iMGLs from iPSCs. We characterize the effect of AD-predisposing genetic backgrounds on the functionality of cells featuring a profound impact of *APOE* on the phenotype of microglia. The current study highlights the importance of investigating the role of gene variants in human microglia and provides a useful, clinically relevant model for studying microglia in disease.

EXPERIMENTAL PROCEDURES

See further details in the Supplemental Experimental Procedures.

Generation and Maintenance of iPSCs

iPSC lines Ctrl1, Ctrl3, and PSEN1, and their isogenic control lines were previously generated and characterized (Oksanen et al., 2017) by the approval of the committee on Research Ethics of Northern Savo Hospital district (123/2016) after written consent from the subjects. pAPP and spAPP lines were approved by the ethical review board of Karolinska Institutet/University (2017/834–31/1), and spAPP was characterized previously (Oksanen et al., 2018). HC1-3 and LOAD1-3 lines were characterized (Balez et al., 2016; Munoz et al., 2018; Ooi et al., 2013) with the approval of the University of Wollongong human research ethics committee (HE13/299). Previously uncharacterized lines pAPP, TOB0002c3, and MBE2968c1 were approved by the ethical review board of Karolinska Institutet/University (2017/834–31/1), or by the human research ethics committees of the Royal Victorian Eye and Ear Hospital (11/1031H, 13/1151H-004), University of Melbourne (1545394), University of Tasmania (H0014124), with the requirements of the National Health & Medical Research Council of Australia and conformed with the Declarations of Helsinki (McCaughey et al., 2016). Fibroblasts were isolated and cultured as described previously (Crombie et al., 2017; Qu et al., 2013) and were reprogrammed to iPSCs either with Sendai virus using CytoTune 1.0 kit (Invitrogen) (Holmqvist et al., 2016) or by nucleofection (Lonza Amaxa Nucleofector) (Okita et al., 2011). iPSCs were maintained in Essential 8 Medium (E8, Gibco) on Matrigel (Corning) and were passaged with 0.5 mM EDTA (Invitrogen) in the presence of 5 μM Y-27632 (Selleckchem). All iPSCs were confirmed to be sterile and all cell cultures were tested for mycoplasma using a MycoAlert Kit (Lonza).

Differentiation of iMGLs

On D0, iPSCs were dissociated to single cells with 0.5 mM EDTA or Accutase (Innovative Cell Technologies) and were replated at a density of 6,000–16,000 cells/cm^2 on Matrigel in E8, 0.5% penicillin/streptomycin (P/S) (50 IU/50 mg/mL), 5 ng/mL BMP4, 25 ng/mL Activin A (both from PeproTech or Miltenyi Biotec), 1 μM CHIR 99021 (Axon or Stem Cell Technologies) and 10 μM Y-27632. The cells were maintained in low oxygen at 5% O_2, 5% CO_2, 37°C. On D1, the medium was replaced with a lower concentration of 1 μM Y-27632. After 48 h on D2 the medium was changed to differentiation base medium (dif-base) containing DMEM/F-12, 0.5% P/S, 1% GlutaMAX, 0.0543% sodium bicarbonate (all from Thermo Fisher Scientific), 64 mg/L L-ascorbic acid and 14 μg/L sodium selenite (both from Sigma). The dif-base was supplemented with 100 ng/mL FGF2, 50 ng/mL VEGF (both from PeproTech), 10 μM SB431542 (Selleckchem or Stem Cell Technologies), and 5 μg/mL insulin (Sigma). On D4, the media was replaced by dif-base supplemented with 5 μg/mL insulin, 50 ng/mL FGF2, VEGF, IL-6, and thyroid peroxidase, and 10 ng/mL IL-3 and stem cell factor. From then on, the cells were maintained in a normoxic incubator. Fresh EMP medium was changed daily until D8, when floating round EMPs were collected from the top of the monolayer. After centrifugation 300 × *g* for 5 min, 350,000 cells/mL were transferred to ULA dishes (Corning) in microglial medium containing Iscove's modified Dulbecco's medium (Thermo Fisher Scientific), 0.5% P/S, and 10% heat inactivated FBS (Biowest) or DMEM/F12, 0.5% N_2, 0.5% B27 supplemented with 5 μg/mL insulin, 5 ng/mL MCSF, and 100 ng/mL IL-34 (both from PeproTech). On D10, the cell suspension was changed by centrifuging and 350,000 cells/mL were seeded back to ULA dishes in microglial maturation medium supplemented with 10 ng/mL MCSF and 10 ng/mL IL-34. This medium was changed similarly every second day until D16, when the cells were detached from ULA dishes with Accutase and replated on PDL-coated (Sigma) nunclon cell culture-treated plates (Thermo Fisher Scientific) in desired densities for experiments. Half of the maturation medium was changed daily until D23–24 when experiments were performed. To ensure the functionality of the cells after longer maturation, iMGLs from *APOE* lines were maturated in presence of IL-34 (100 ng/mL) and MCSF (5 ng/mL) until D42, and similar results were obtained for cytokine secretion, qRT-PCR and phagocytosis.

Statistical Analysis

Statistical analysis was performed using Graphpad Prism 7. Comparisons involving two groups were analyzed with two-tailed Student's t test. One-way ANOVA was utilized for comparisons with more than two groups followed by Tukey's post hoc test. Two-way ANOVA was utilized for comparisons of genotypes and treatment groups and followed by Bonferroni's multiple-comparison post hoc test. Corrected p values for multiple comparisons were reported. Differences were considered significant when $p < 0.05$.

ACCESSION NUMBERS

The accession number for the RNA sequencing data generated in this paper is GEO: GSE135707. The datasets reanalyzed for this study are available through GEO: GSE89189 (Abud et al., 2017).

SUPPLEMENTAL INFORMATION

Supplemental Information can be found online at https://doi.org/10.1016/j.stemcr.2019.08.004.

AUTHOR CONTRIBUTIONS

H.K. and M.C.-S. designed and performed the experiments and analyzed the data. T.M., L.O., K.M.K., and H.K. conceived and designed the study. T.M. and H.K. developed the differentiation method of iMGLs with guidance from M.P.S. and N.P. T.M., H.K., L.O., and M.C.-S. supervised experiments and interpreted the results. D.H., A.P., A.W.H., J.V., C.G., G.C.S., S.L., J.K., and M.O. generated and characterized iPSCs lines. H.K. and M.C.-S. cultured the iPSCs and iMGLs with input from S.O., S.E., M.G.B., I.F., P.K., and M.F.F. R.G., S.C., and M.F.F. performed transcriptome analysis. I.F. developed the 3D brain organoids and M.O. prepared neuronal 3D-cultures. Y.I. and A.S. did calcium imaging. H.K. and S.W. conducted flow cytometer analysis with input from F.S. N.H., and A.W.H. performed western blots. H.K., T.M., L.O., and M.C.-S. interpreted the data and wrote the paper, while all authors provided feedback.

ACKNOWLEDGMENTS

This work is part of an EU Joint Program – Neurodegenerative Disease Research (JPND) project. This study was funded by the University of Eastern Finland, the Academy of Finland under grant nos. 301234, 298071, 305516, and 315459 (FiNeFTD), the European Union's Horizon 2020 research and innovation program under grant agreement no. 643417, Finnish Instrumentarium Science Foundation, and Yrjö Jahnsson's Foundation grant no. 20187070, the National Health and Medical Research Council of Australia (NHMRC, APP1125796), an NHMRC Boosting Dementia Research Leadership Fellowship (APP1135720), Yulgilbar Alzheimer's Research Program, the DHB Foundation, the C.F. Leung Memorial Trust, the Brain Foundation, Dementia Australia, a National Health and Medical Research Council Practitioner Fellowship (AWH) and Senior Research Fellowship (AP, 1154389), an Australian Research Council Future Fellowship (AP, FT140100047), the University of Melbourne and Operational Infrastructure Support from the Victorian Government. We thank Matti Viitala for skin biopsies, Louise A. Rooney, Sophie Chevalier, and Maciej Daniszewski for the characterization of iPSC lines, Vikrant Singh for virtual karyotype help, and Helena H. Liang for culture of biopsies to fibroblasts. We also thank Finnish Functional Genomics Center (FFGC), University of Turku and Åbo Akademi and Biocenter Finland, for RNA sequencing. This work was carried out with the support of UEF Cell and Tissue Imaging Unit, University of Eastern Finland.

Received: April 15, 2019
Revised: August 14, 2019
Accepted: August 15, 2019
Published: September 12, 2019

REFERENCES

Abud, E.M., Ramirez, R.N., Martinez, E.S., Healy, L.M., Nguyen, C.H.H., Newman, S.A., Yeromin, A.V., Scarfone, V.M., Marsh, S.E., Fimbres, C., et al. (2017). iPSC-derived human microglia-like cells to study neurological diseases. Neuron *94*, 278–293.e9.

Bagyinszky, E., Youn, Y.C., An, S.S., and Kim, S. (2014). The genetics of Alzheimer's disease. Clin. Interv. Aging *9*, 535–551.

Balez, R., Steiner, N., Engel, M., Munoz, S.S., Lum, J.S., Wu, Y., Wang, D., Vallotton, P., Sachdev, P., O'Connor, M., et al. (2016). Neuroprotective effects of apigenin against inflammation, neuronal excitability and apoptosis in an induced pluripotent stem cell model of Alzheimer's disease. Sci. Rep. *6*, 31450.

Banati, R.B., Gehrmann, J., Czech, C., Monning, U., Jones, L.L., Konig, G., Beyreuther, K., and Kreutzberg, G.W. (1993). Early and rapid de novo synthesis of Alzheimer beta A4-amyloid precursor protein (APP) in activated microglia. Glia *9*, 199–210.

Barroeta-Espar, I., Weinstock, L.D., Perez-Nievas, B.G., Meltzer, A.C., Siao Tick Chong, M., Amaral, A.C., Murray, M.E., Moulder, K.L., Morris, J.C., Cairns, N.J., et al. (2019). Distinct cytokine profiles in human brains resilient to Alzheimer's pathology. Neurobiol. Dis. *121*, 327–337.

Bennett, M.L., Bennett, F.C., Liddelow, S.A., Ajami, B., Zamanian, J.L., Fernhoff, N.B., Mulinyawe, S.B., Bohlen, C.J., Adil, A., Tucker, A., et al. (2016). New tools for studying microglia in the mouse and human CNS. Proc. Natl. Acad. Sci. U S A *113*, E1738–E1746.

Butovsky, O., Jedrychowski, M.P., Moore, C.S., Cialic, R., Lanser, A.J., Gabriely, G., Koeglsperger, T., Dake, B., Wu, P.M., Doykan, C.E., et al. (2014). Identification of a unique TGF-beta-dependent molecular and functional signature in microglia. Nat. Neurosci. *17*, 131–143.

Caldeira, C., Cunha, C., Vaz, A.R., Falcao, A.S., Barateiro, A., Seixas, E., Fernandes, A., and Brites, D. (2017). Key aging-associated alterations in primary microglia response to beta-amyloid stimulation. Front. Aging Neurosci. *9*, 277.

Colonna, M., and Butovsky, O. (2017). Microglia function in the central nervous system during health and neurodegeneration. Annu. Rev. Immunol. *35*, 441–468.

Crombie, D.E., Daniszewski, M., Liang, H.H., Kulkarni, T., Li, F., Lidgerwood, G.E., Conquest, A., Hernandez, D., Hung, S.S., Gill, K.P., et al. (2017). Development of a modular automated system for maintenance and differentiation of adherent human pluripotent stem cells. SLAS Discov. *22*, 1016–1025.

Crook, R., Verkkoniemi, A., Perez-Tur, J., Mehta, N., Baker, M., Houlden, H., Farrer, M., Hutton, M., Lincoln, S., Hardy, J., et al. (1998). A variant of Alzheimer's disease with spastic paraparesis and unusual plaques due to deletion of exon 9 of presenilin 1. Nat. Med. *4*, 452–455.

De Simone, R., Niturad, C.E., De Nuccio, C., Ajmone-Cat, M.A., Visentin, S., and Minghetti, L. (2010). TGF-beta and LPS modulate ADP-induced migration of microglial cells through P2Y1 and P2Y12 receptor expression. J. Neurochem. *115*, 450–459.

Douvaras, P., Sun, B., Wang, M., Kruglikov, I., Lallos, G., Zimmer, M., Terrenoire, C., Zhang, B., Gandy, S., Schadt, E., et al. (2017). Directed differentiation of human pluripotent stem cells to Microglia. Stem Cell Reports *8*, 1516–1524.

Engel, M., Balez, R., Munoz, S.S., Cabral-da-Silva, M.C., Stevens, C.H., Bax, M., Do-Ha, D., Sidhu, K., Sachdev, P., and Ooi, L. (2018). Viral-free generation and characterization of a human induced pluripotent stem cell line from dermal fibroblasts. Stem Cell Res. *32*, 135–138.

Ghosh, S., Castillo, E., Frias, E.S., and Swanson, R.A. (2018). Bioenergetic regulation of microglia. Glia *66*, 1200–1212.

Ginhoux, F., Greter, M., Leboeuf, M., Nandi, S., See, P., Gokhan, S., Mehler, M.F., Conway, S.J., Ng, L.G., Stanley, E.R., et al. (2010). Fate mapping analysis reveals that adult microglia derive from primitive macrophages. Science *330*, 841–845.

Ginhoux, F., Lim, S., Hoeffel, G., Low, D., and Huber, T. (2013). Origin and differentiation of microglia. Front. Cell Neurosci. *7*, 45.

Haenseler, W., Sansom, S.N., Buchrieser, J., Newey, S.E., Moore, C.S., Nicholls, F.J., Chintawar, S., Schnell, C., Antel, J.P., Allen, N.D., et al. (2017). A highly efficient human pluripotent stem cell Microglia model displays a neuronal-co-culture-specific expression profile and inflammatory response. Stem Cell Reports *8*, 1727–1742.

Hoffmann, A., Kann, O., Ohlemeyer, C., Hanisch, U.K., and Kettenmann, H. (2003). Elevation of basal intracellular calcium as a central element in the activation of brain macrophages (microglia): suppression of receptor-evoked calcium signaling and control of release function. J. Neurosci. *23*, 4410–4419.

Holmqvist, S., Lehtonen, S., Chumarina, M., Puttonen, K.A., Azevedo, C., Lebedeva, O., Ruponen, M., Oksanen, M., Djelloul, M., Collin, A., et al. (2016). Creation of a library of induced pluripotent stem cells from Parkinsonian patients. NPJ Parkinson's Dis. *2*, 16009.

Jayadev, S., Case, A., Alajajian, B., Eastman, A.J., Moller, T., and Garden, G.A. (2013). Presenilin 2 influences miR146 level and activity in microglia. J. Neurochem. *127*, 592–599.

Kennedy, M., D'Souza, S.L., Lynch-Kattman, M., Schwantz, S., and Keller, G. (2007). Development of the hemangioblast defines the onset of hematopoiesis in human ES cell differentiation cultures. Blood *109*, 2679–2687.

Kierdorf, K., Erny, D., Goldmann, T., Sander, V., Schulz, C., Perdiguero, E.G., Wieghofer, P., Heinrich, A., Riemke, P., Holscher, C., et al. (2013). Microglia emerge from erythromyeloid precursors via Pu.1- and Irf8-dependent pathways. Nat. Neurosci. *16*, 273–280.

Koenigsknecht-Talboo, J., and Landreth, G.E. (2005). Microglial phagocytosis induced by fibrillar beta-amyloid and IgGs are differentially regulated by proinflammatory cytokines. J. Neurosci. *25*, 8240–8249.

Krasemann, S., Madore, C., Cialic, R., Baufeld, C., Calcagno, N., El Fatimy, R., Beckers, L., O'Loughlin, E., Xu, Y., Fanek, Z., et al. (2017). The TREM2-APOE pathway drives the transcriptional phenotype of dysfunctional microglia in neurodegenerative diseases. Immunity *47*, 566–581.e9.

Lambert, C., Ase, A.R., Seguela, P., and Antel, J.P. (2010). Distinct migratory and cytokine responses of human microglia and macrophages to ATP. Brain Behav. Immun. *24*, 1241–1248.

Lanzrein, A.S., Johnston, C.M., Perry, V.H., Jobst, K.A., King, E.M., and Smith, A.D. (1998). Longitudinal study of inflammatory factors in serum, cerebrospinal fluid, and brain tissue in Alzheimer disease: interleukin-1beta, interleukin-6, interleukin-1 receptor antagonist, tumor necrosis factor-alpha, the soluble tumor necrosis factor receptors I and II, and alpha1-antichymotrypsin. Alzheimer Dis. Assoc. Disord. *12*, 215–227.

Lavin, Y., Winter, D., Blecher-Gonen, R., David, E., Keren-Shaul, H., Merad, M., Jung, S., and Amit, I. (2014). Tissue-resident macrophage enhancer landscapes are shaped by the local microenvironment. Cell *159*, 1312–1326.

Lee, C.Y., and Landreth, G.E. (2010). The role of microglia in amyloid clearance from the AD brain. J. Neural Transm. (Vienna) *117*, 949–960.

Lin, Y.T., Seo, J., Gao, F., Feldman, H.M., Wen, H.L., Penney, J., Cam, H.P., Gjoneska, E., Raja, W.K., Cheng, J., et al. (2018). APOE4 causes widespread molecular and cellular alterations associated with Alzheimer's disease phenotypes in human iPSC-derived brain cell types. Neuron *98*, 1141–1154.e7.

Liu, C.C., Liu, C.C., Kanekiyo, T., Xu, H., and Bu, G. (2013). Apolipoprotein E and Alzheimer disease: risk, mechanisms and therapy. Nat. Rev. Neurol. *9*, 106–118.

Manocha, G.D., Floden, A.M., Rausch, K., Kulas, J.A., McGregor, B.A., Rojanathammanee, L., Puig, K.R., Puig, K.L., Karki, S., Nichols, M.R., et al. (2016). APP regulates microglial phenotype in a mouse model of Alzheimer's disease. J. Neurosci. *36*, 8471–8486.

McCaughey, T., Liang, H.H., Chen, C., Fenwick, E., Rees, G., Wong, R.C., Vickers, J.C., Summers, M.J., MacGregor, C., Craig, J.E., et al. (2016). An interactive multimedia approach to improving informed consent for induced pluripotent stem cell research. Cell Stem Cell *18*, 307–308.

McQuade, A., Coburn, M., Tu, C.H., Hasselmann, J., Davtyan, H., and Blurton-Jones, M. (2018). Development and validation of a simplified method to generate human microglia from pluripotent stem cells. Mol. Neurodegener. *13*, 67.

Muffat, J., Li, Y., Yuan, B., Mitalipova, M., Omer, A., Corcoran, S., Bakiasi, G., Tsai, L.H., Aubourg, P., Ransohoff, R.M., et al. (2016). Efficient derivation of microglia-like cells from human pluripotent stem cells. Nat. Med. *22*, 1358–1367.

Mullan, M., Crawford, F., Axelman, K., Houlden, H., Lilius, L., Winblad, B., and Lannfelt, L. (1992). A pathogenic mutation for probable Alzheimer's disease in the APP gene at the N-terminus of beta-amyloid. Nat. Genet. *1*, 345–347.

Munoz, S.S., Balez, R., Castro Cabral-da-Silva, M.E., Berg, T., Engel, M., Bax, M., Do-Ha, D., Stevens, C.H., Greenough, M., Bush, A., et al. (2018). Generation and characterization of human induced pluripotent stem cell lines from a familial Alzheimer's disease PSEN1 A246E patient and a non-demented family member bearing wild-type PSEN1. Stem Cell Res. *31*, 227–230.

Nadler, Y., Alexandrovich, A., Grigoriadis, N., Hartmann, T., Rao, K.S., Shohami, E., and Stein, R. (2008). Increased expression of the gamma-secretase components presenilin-1 and nicastrin in activated astrocytes and microglia following traumatic brain injury. Glia *56*, 552–567.

Oberstein, T.J., Spitzer, P., Klafki, H.W., Linning, P., Neff, F., Knolker, H.J., Lewczuk, P., Wiltfang, J., Kornhuber, J., and Maler, J.M. (2015). Astrocytes and microglia but not neurons preferentially generate N-terminally truncated Abeta peptides. Neurobiol. Dis. *73*, 24–35.

Okita, K., Matsumura, Y., Sato, Y., Okada, A., Morizane, A., Okamoto, S., Hong, H., Nakagawa, M., Tanabe, K., Tezuka, K.,

et al. (2011). A more efficient method to generate integration-free human iPS cells. Nat. Methods *8*, 409–412.

Oksanen, M., Hyotylainen, I., Voutilainen, J., Puttonen, K.A., Hamalainen, R.H., Graff, C., Lehtonen, S., and Koistinaho, J. (2018). Generation of a human induced pluripotent stem cell line (LL008 1.4) from a familial Alzheimer's disease patient carrying a double KM670/671NL (Swedish) mutation in APP gene. Stem Cell Res. *31*, 181–185.

Oksanen, M., Petersen, A.J., Naumenko, N., Puttonen, K., Lehtonen, S., Gubert Olive, M., Shakirzyanova, A., Leskela, S., Sarajarvi, T., Viitanen, M., et al. (2017). PSEN1 mutant iPSC-derived model reveals severe astrocyte pathology in Alzheimer's disease. Stem Cell Reports *9*, 1885–1897.

Olah, M., Patrick, E., Villani, A.C., Xu, J., White, C.C., Ryan, K.J., Piehowski, P., Kapasi, A., Nejad, P., Cimpean, M., et al. (2018). A transcriptomic atlas of aged human microglia. Nat. Commun. *9*, 539.

Ooi, L., Sidhu, K., Poljak, A., Sutherland, G., O'Connor, M.D., Sachdev, P., and Munch, G. (2013). Induced pluripotent stem cells as tools for disease modelling and drug discovery in Alzheimer's disease. J. Neural Transm. (Vienna) *120*, 103–111.

Orihuela, R., McPherson, C.A., and Harry, G.J. (2016). Microglial M1/M2 polarization and metabolic states. Br. J. Pharmacol. *173*, 649–665.

Pandya, H., Shen, M.J., Ichikawa, D.M., Sedlock, A.B., Choi, Y., Johnson, K.R., Kim, G., Brown, M.A., Elkahloun, A.G., Maric, D., et al. (2017). Differentiation of human and murine induced pluripotent stem cells to microglia-like cells. Nat. Neurosci. *20*, 753–759.

Pulido-Salgado, M., Vidal-Taboada, J.M., Barriga, G.G., Sola, C., and Saura, J. (2018). RNA-Seq transcriptomic profiling of primary murine microglia treated with LPS or LPS + IFNgamma. Sci. Rep. *8*, 16096.

Qu, C., Puttonen, K.A., Lindeberg, H., Ruponen, M., Hovatta, O., Koistinaho, J., and Lammi, M.J. (2013). Chondrogenic differentiation of human pluripotent stem cells in chondrocyte co-culture. Int. J. Biochem. Cell Biol. *45*, 1802–1812.

Rustenhoven, J., Park, T.I., Schweder, P., Scotter, J., Correia, J., Smith, A.M., Gibbons, H.M., Oldfield, R.L., Bergin, P.S., Mee, E.W., et al. (2016). Isolation of highly enriched primary human microglia for functional studies. Sci. Rep. *6*, 19371.

Saijo, K., and Glass, C.K. (2011). Microglial cell origin and phenotypes in health and disease. Nat. Rev. Immunol. *11*, 775–787.

Scheuner, D., Eckman, C., Jensen, M., Song, X., Citron, M., Suzuki, N., Bird, T.D., Hardy, J., Hutton, M., Kukull, W., et al. (1996). Secreted amyloid beta-protein similar to that in the senile plaques of Alzheimer's disease is increased in vivo by the presenilin 1 and 2 and APP mutations linked to familial Alzheimer's disease. Nat. Med. *2*, 864–870.

Schwartz, M.P., Hou, Z., Propson, N.E., Zhang, J., Engstrom, C.J., Santos Costa, V., Jiang, P., Nguyen, B.K., Bolin, J.M., Daly, W., et al. (2015). Human pluripotent stem cell-derived neural constructs for predicting neural toxicity. Proc. Natl. Acad. Sci. U S A *112*, 12516–12521.

Selkoe, D.J. (1998). The cell biology of beta-amyloid precursor protein and presenilin in Alzheimer's disease. Trends Cell Biol. *8*, 447–453.

Shi, Y., and Holtzman, D.M. (2018). Interplay between innate immunity and Alzheimer disease: APOE and TREM2 in the spotlight. Nat. Rev. Immunol. *18*, 759–772.

Smith, J.A., Das, A., Ray, S.K., and Banik, N.L. (2012). Role of pro-inflammatory cytokines released from microglia in neurodegenerative diseases. Brain Res. Bull. *87*, 10–20.

Sturgeon, C.M., Ditadi, A., Awong, G., Kennedy, M., and Keller, G. (2014). Wnt signaling controls the specification of definitive and primitive hematopoiesis from human pluripotent stem cells. Nat. Biotechnol. *32*, 554–561.

Ta, T.T., Dikmen, H.O., Schilling, S., Chausse, B., Lewen, A., Hollnagel, J.O., and Kann, O. (2019). Priming of microglia with IFN-gamma slows neuronal gamma oscillations in situ. Proc. Natl. Acad. Sci. U S A. https://doi.org/10.1073/pnas.1813562116.

Townsend, K.P., Town, T., Mori, T., Lue, L.F., Shytle, D., Sanberg, P.R., Morgan, D., Fernandez, F., Flavell, R.A., and Tan, J. (2005). CD40 signaling regulates innate and adaptive activation of microglia in response to amyloid beta-peptide. Eur. J. Immunol. *35*, 901–910.

Uenishi, G., Theisen, D., Lee, J.H., Kumar, A., Raymond, M., Vodyanik, M., Swanson, S., Stewart, R., Thomson, J., and Slukvin, I. (2014). Tenascin C promotes hematoendothelial development and T lymphoid commitment from human pluripotent stem cells in chemically defined conditions. Stem Cell Reports *3*, 1073–1084.

Ulland, T.K., Song, W.M., Huang, S.C., Ulrich, J.D., Sergushichev, A., Beatty, W.L., Loboda, A.A., Zhou, Y., Cairns, N.J., Kambal, A., et al. (2017). TREM2 maintains microglial metabolic fitness in Alzheimer's disease. Cell *170*, 649–663.e13.

Wang, W.Y., Tan, M.S., Yu, J.T., and Tan, L. (2015). Role of pro-inflammatory cytokines released from microglia in Alzheimer's disease. Ann. Transl. Med. *3*, 136.

Weuve, J., Hebert, L.E., Scherr, P.A., and Evans, D.A. (2014). Deaths in the United States among persons with Alzheimer's disease (2010-2050). Alzheimers Dement. *10*, e40–e46.

Xu, M., Zhang, L., Liu, G., Jiang, N., Zhou, W., and Zhang, Y. (2019). Pathological changes in alzheimer's disease analyzed using induced pluripotent stem cell-derived human Microglia-like cells. J. Alzheimers Dis. *67*, 357–368.

Zhang, Y., Chen, K., Sloan, S.A., Bennett, M.L., Scholze, A.R., O'Keeffe, S., Phatnani, H.P., Guarnieri, P., Caneda, C., Ruderisch, N., et al. (2014). An RNA-sequencing transcriptome and splicing database of glia, neurons, and vascular cells of the cerebral cortex. J. Neurosci. *34*, 11929–11947.

Zhao, Y., Li, X., Huang, T., Jiang, L.L., Tan, Z., Zhang, M., Cheng, I.H., Wang, X., Bu, G., Zhang, Y.W., et al. (2017). Intracellular trafficking of TREM2 is regulated by presenilin 1. Exp. Mol. Med. *49*, e405.

Stem Cell Reports, Volume *13*

Supplemental Information

*PSEN1*ΔE9, *APPswe*, and *APOE4* Confer Disparate Phenotypes in Human iPSC-Derived Microglia

Henna Konttinen, Mauricio e Castro Cabral-da-Silva, Sohvi Ohtonen, Sara Wojciechowski, Anastasia Shakirzyanova, Simone Caligola, Rosalba Giugno, Yevheniia Ishchenko, Damián Hernández, Mohammad Feroze Fazaludeen, Shaila Eamen, Mireia Gómez Budia, Ilkka Fagerlund, Flavia Scoyni, Paula Korhonen, Nadine Huber, Annakaisa Haapasalo, Alex W. Hewitt, James Vickers, Grady C. Smith, Minna Oksanen, Caroline Graff, Katja M. Kanninen, Sarka Lehtonen, Nicholas Propson, Michael P. Schwartz, Alice Pébay, Jari Koistinaho, Lezanne Ooi, and Tarja Malm

Supplemental Figures

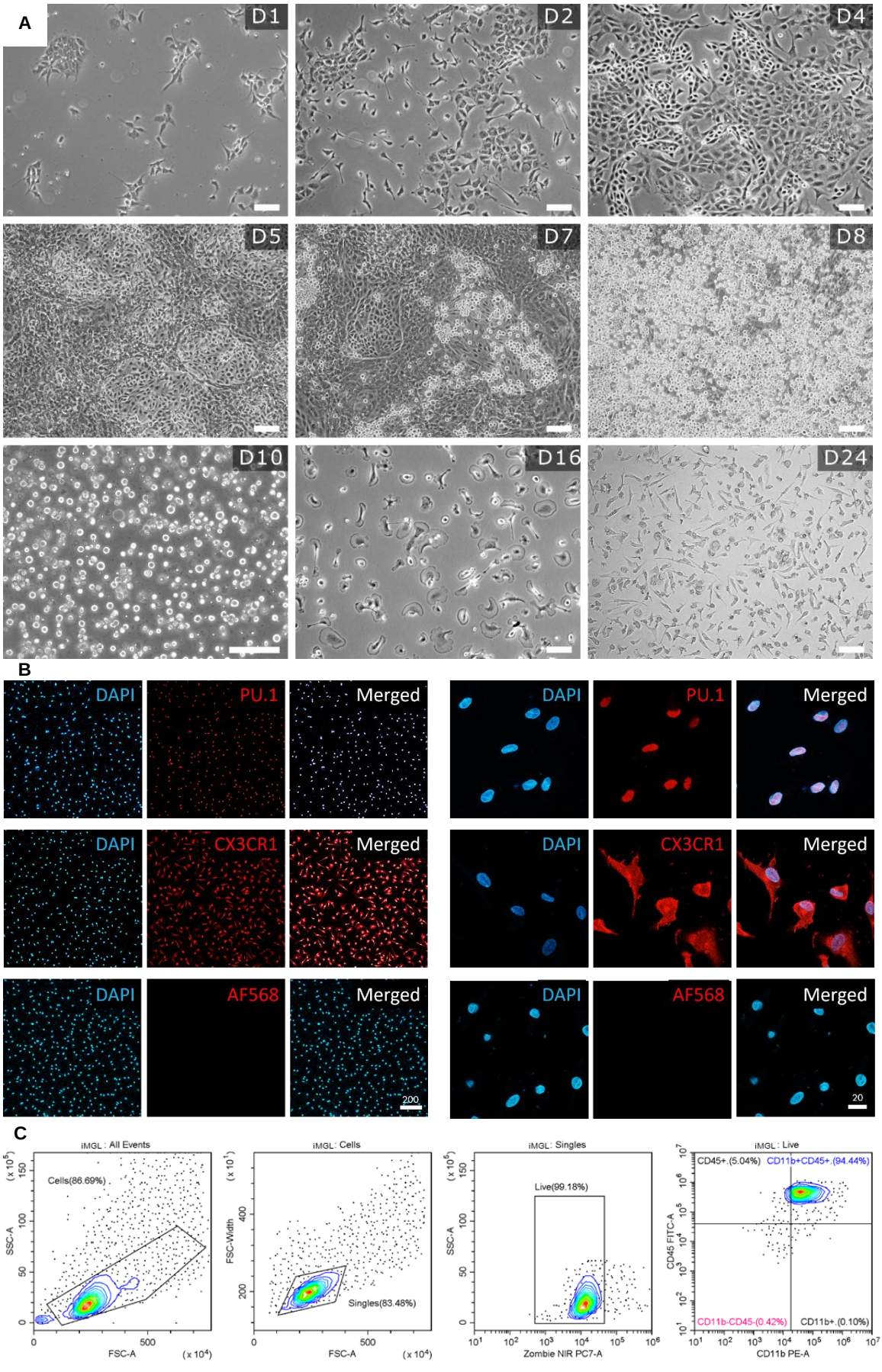

Figure S1. Microglial identity of iMGLs. Related to Figure 1.
(A) Morphological changes during iMGL differentiation presented as bright field images taken using ZEISS IX70 microscope with Axio Observer.Z1 (ZEISS) with 5X magnification. D1-D8 present images from Matrigel dishes, D10 and D16 on ULA-dishes and D24 shows the cells on PDL-coating. When the cells were maintained on ULA dishes after D16, they continued to have lamellipodia as presented in D16 image, whereas on PDL-coated vessels, the cells adopted more ramified and elongated morphology as presented on D24 image. Scale bar 100 µm. **(B)** Representative immunocytochemistry images of D24 iMGLs labeled with DAPI (blue) and PU.1 (red), CX3CR1 (red), or only with secondary antibody AF568 as a negative control with no primary antibody. Scale bar µm. **(C)** Representative gating strategy for flow analysis for CD11b-PE and CD45-FITC double stained D24 iMGLs.

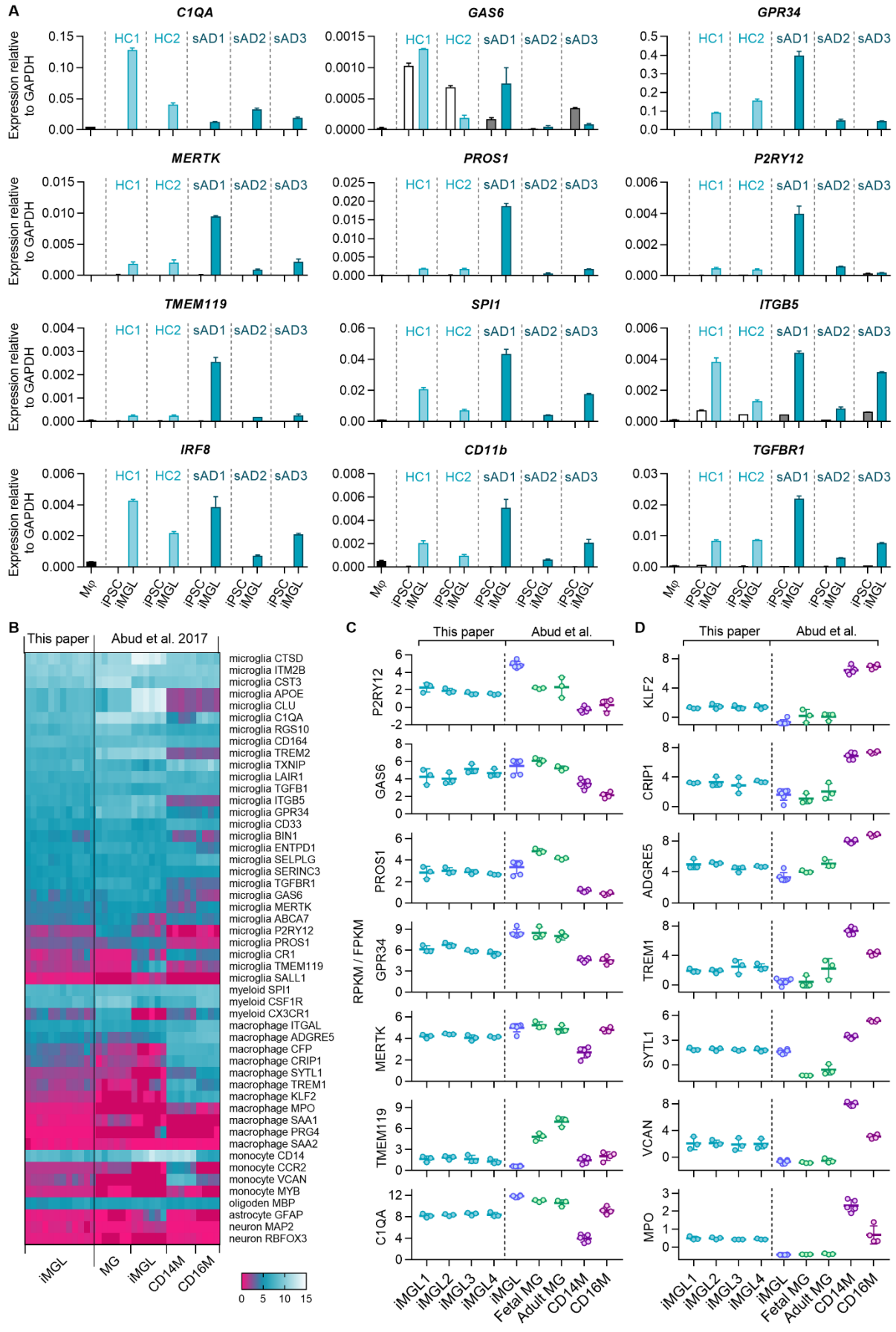
A
C1QA
GAS6
GPR34
MERTK
PROS1
P2RY12
TMEM119
SPI1
ITGB5
IRF8
CD11b
TGFBR1
Expression relative to GAPDH
HC1
HC2
sAD1
sAD2
sAD3
Mφ
iPSC
iMGL
B
This paper
Abud et al. 2017
microglia CTSD
microglia ITM2B
microglia CST3
microglia APOE
microglia CLU
microglia C1QA
microglia RGS10
microglia CD164
microglia TREM2
microglia TXNIP
microglia LAIR1
microglia TGFB1
microglia ITGB5
microglia GPR34
microglia CD33
microglia BIN1
microglia ENTPD1
microglia SELPLG
microglia SERINC3
microglia TGFBR1
microglia GAS6
microglia MERTK
microglia ABCA7
microglia P2RY12
microglia PROS1
microglia CR1
microglia TMEM119
microglia SALL1
myeloid SPI1
myeloid CSF1R
myeloid CX3CR1
macrophage ITGAL
macrophage ADGRE5
macrophage CFP
macrophage CRIP1
macrophage SYTL1
macrophage TREM1
macrophage KLF2
macrophage MPO
macrophage SAA1
macrophage PRG4
macrophage SAA2
monocyte CD14
monocyte CCR2
monocyte VCAN
monocyte MYB
oligoden MBP
astrocyte GFAP
neuron MAP2
neuron RBFOX3
iMGL
MG
iMGL
CD14M
CD16M
0 5 10 15
C
This paper
Abud et al.
RPKM / FPKM
P2RY12
GAS6
PROS1
GPR34
MERTK
TMEM119
C1QA
iMGL1
iMGL2
iMGL3
iMGL4
iMGL
Fetal MG
Adult MG
CD14M
CD16M
D
This paper
Abud et al.
KLF2
CRIP1
ADGRE5
TREM1
SYTL1
VCAN
MPO
iMGL1
iMGL2
iMGL3
iMGL4
iMGL
Fetal MG
Adult MG
CD14M
CD16M

Figure S2. Microglial gene expression. Related to Figure 1.
qRT-PCR and RNA-seq verifies that iMGL represent microglia-like gene expression and transcriptomic profile and cluster together with human microglia. **(A)** The qRT-PCR of 12 microglial signature genes was analyzed relative to GAPDH from RNA harvested from iPSCs and iMGLs as well as from human PBMC-derived CD14+ macrophages (Mφ). Representative data from two healthy control (HC) and three symptomatic LOAD (sAD) lines shown. n=3 technical replicates, repeated in three experiments. **(B)** Heat map of the RPKM/FPKM values from RNAseq data show that multiple microglial genes are highly expressed whereas macrophage genes are expressed at lower levels in iMGLs of this paper and (Abud et al., 2017) iMGLs and primary microglia (MG) compared to CD14M and CD16M monocytes/macrophages. ISO, isogenic. n=12 iMGLs including 4 cell lines from 3 batches. For further details, see Supplemental Experimental Procedures. (C) Corresponding bar figures for RPKM/FPKM values of microglial signature genes. (D) Corresponding bar figures for macrophage genes.

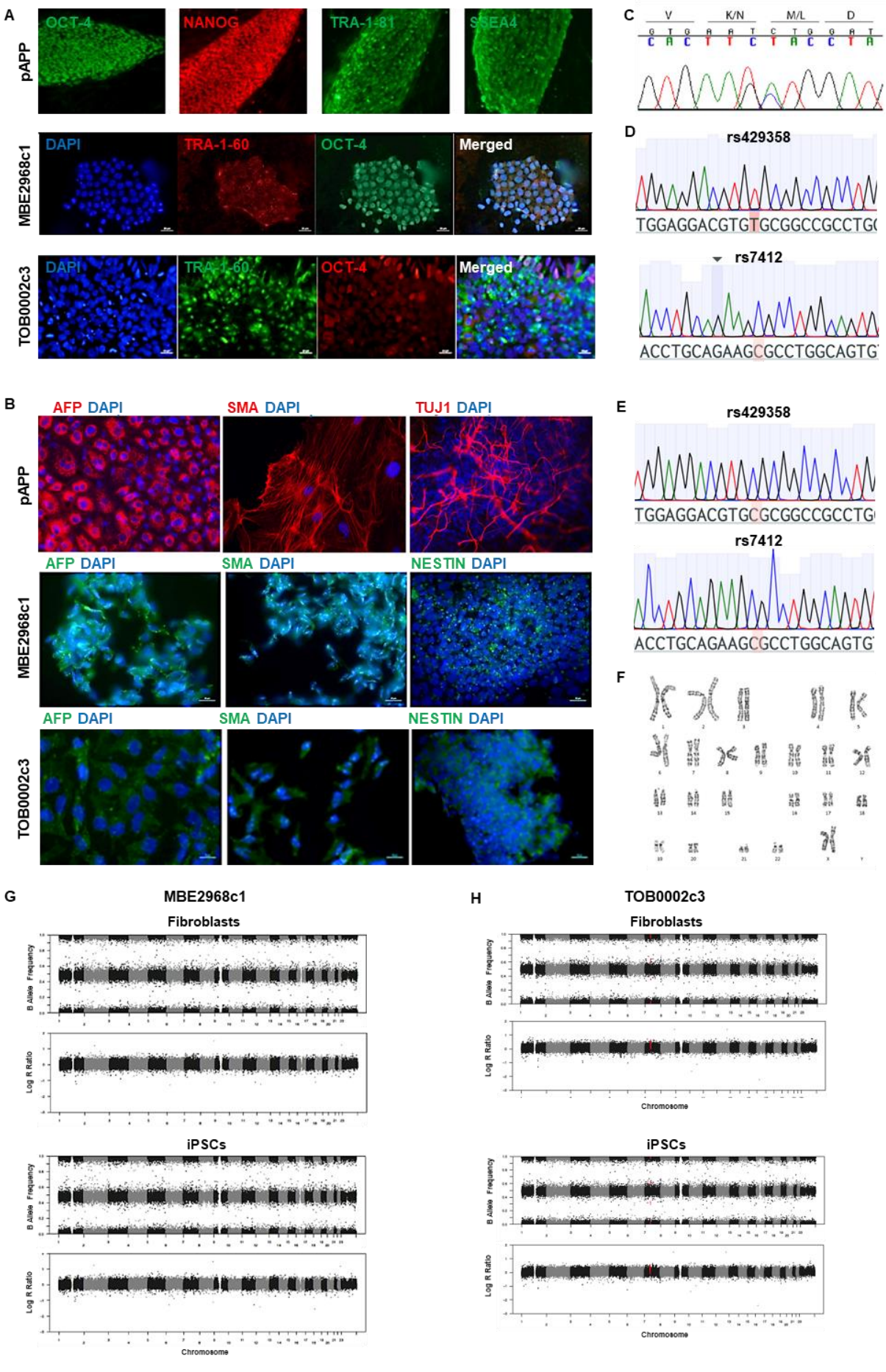
A
pAPP
OCT-4
NANOG
TRA-1-81
SSEA4
MBE2968c1
DAPI
TRA-1-60
OCT-4
Merged
TOB0002c3
DAPI
TRA-1-60
OCT-4
Merged
B
AFP DAPI
SMA DAPI
TUJ1 DAPI
pAPP
AFP DAPI
SMA DAPI
NESTIN DAPI
MBE2968c1
AFP DAPI
SMA DAPI
NESTIN DAPI
TOB0002c3
C
V
K/N
M/L
D
D
rs429358
TGGAGGACGTGTGCGGCCGCCTG
rs7412
ACCTGCAGAAGCGCCTGGCAGTG
E
rs429358
TGGAGGACGTGCGCGGCCGCCTG
rs7412
ACCTGCAGAAGCGCCTGGCAGTG
F
G
MBE2968c1
Fibroblasts
B Allele Frequency
Log R Ratio
iPSCs
B Allele Frequency
Log R Ratio
Chromosome
H
TOB0002c3
Fibroblasts
B Allele Frequency
Log R Ratio
Chromosome
iPSCs
B Allele Frequency
Log R Ratio
Chromosome

Figure S3. Characterization of pluripotency of pAPP, MBE2968c1 and TOB0002c iPSC cell lines. Related to Figure 2.

(A) Representative images of showing expression of the pluripotency markers TRA-1-81, NANOG, SSEA4TRA-1-60 or OCT4. **(B)** Representative germ layer immunostaining for clones differentiated to endoderm (AFP), mesoderm (SMA) and ectoderm (TUJ1 or NESTIN). Genomic Sanger sequencing of **(C)** pAPP showing a double mutation *APP KM670/671NL* (Swedish) at rs63751263 and rs63750445. Sanger sequencing for *APOE* at rs429358 and rs7412 loci confirming **(D)** *APOE3/3* status of MBE2968c1 and **(E)** *APOE4/4* status of TOB0002c3. **(F)** Karyotype of pAPP iPSCs. Copy Number Variation Analysis of the original fibroblasts and iPSCs (p8) for **(G)** MBE2968c1 and **(H)** TOB0002c3. Each panel shows the B allele frequency (BAF) and the log R ratio (LRR). BAF at values others then 0, 0.5 or 1 indicate an abnormal copy number. Similarly, the LRR represents a logged ratio of "observed probe intensity to expected intensity". A deviation from zero corresponds to a change in copy number. See also Table S3.

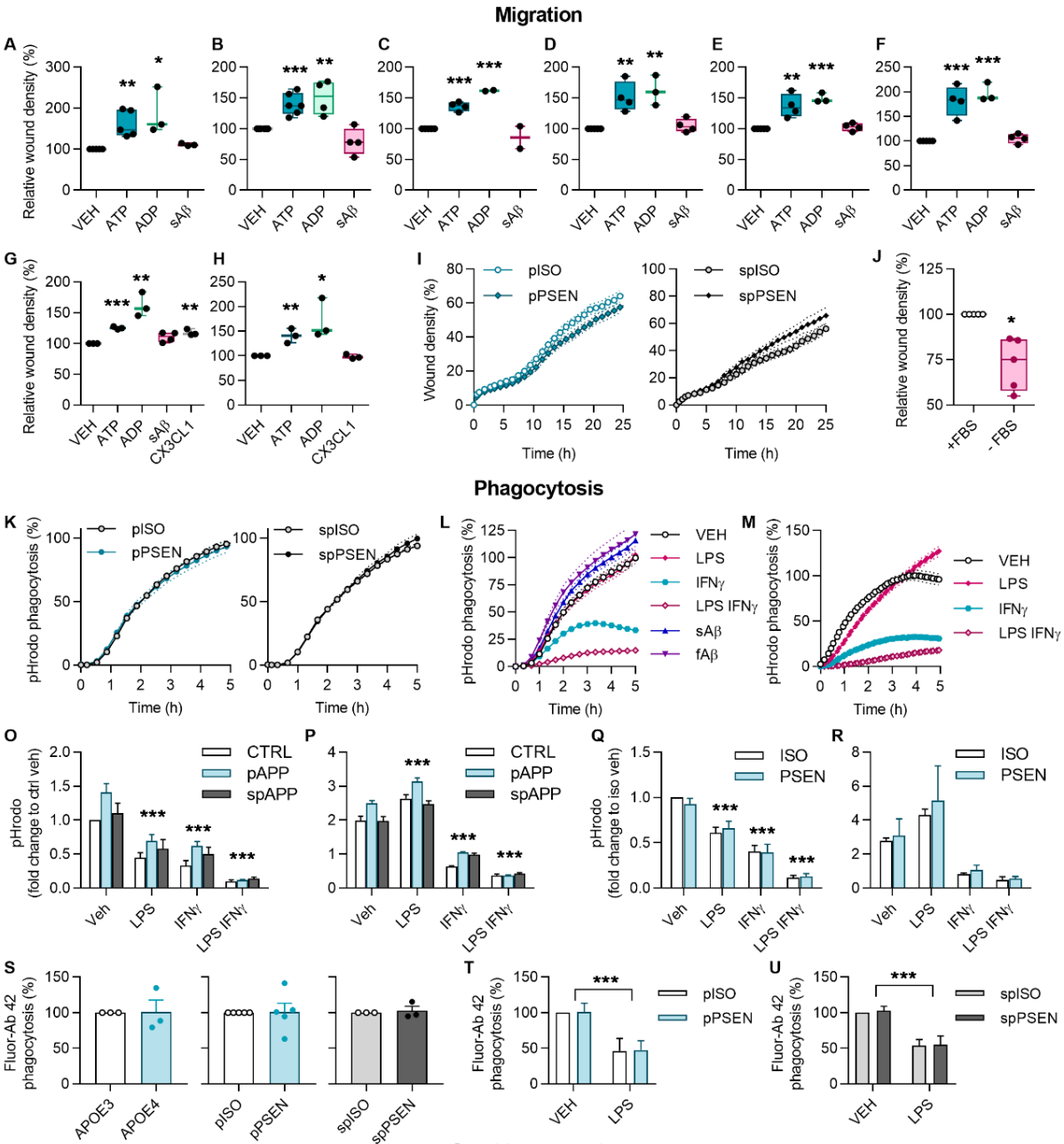
Migration
A
B
C
D
E
F
Relative wound density (%)
VEH
ATP
ADP
sAβ
G
H
CX3CL1
I
pISO
pPSEN
spISO
spPSEN
Wound density (%)
Time (h)
J
+FBS
-FBS
Phagocytosis
K
L
M
pHrodo phagocytosis (%)
VEH
LPS
IFNγ
LPS IFNγ
sAβ
fAβ
O
P
Q
R
pHrodo
(fold change to ctrl veh)
CTRL
pAPP
spAPP
Veh
(fold change to iso veh)
ISO
PSEN
S
T
U
Fluor-Ab 42
phagocytosis (%)
APOE3
APOE4
Cytokine secretion
V
W
X
Y
LPS-induced cytokine
(fold change)
IFNγ-induced cytokine
IL-6
TNFα
MCP1
RANTES
IL-8

Figure S4. Scratch wound migration, phagocytosis and cytokine secretion. Related to Figures 4-6.
Quantification of relative wound density in response to 100 µM ADP, ATP or fractalkine (CX3CL1) and 1 µM sAβ treatments normalized to vehicle (VEH). **(A)** healthy control, **(B)** pre-symptomatic *APPswe* **(C)** symptomatic *APPswe*, **(D))** isogenic control of symptomatic *PSEN1ΔE9*, **(E)** symptomatic *PSEN1ΔE9*, **(F)** pre-symptomatic *PSEN1ΔE9*, **(G)** *APOE3*, and for **(H)** *APOE4* iMGLs (n=2-6 batches, each with 4-5 wells). **(I)** Representative curves for wound density show no differences between *PSEN1ΔE9* and isogenic control iMGLs. n=4 wells. **(K)** Withdrawal of FBS (-FBS) reduced migration for 27% compared to normal medium (+FBS) at 25h. n=5 batches, each with 4-5 wells. **(K)** Representative curves for Zymosan A pHrodo phagocytosis in pre-symptomatic and symptomatic *PSEN1ΔE9* iMGLs and their isogenic controls. **(L)** Representative curves for pHrodo phagocytosis in control iMGLs with 24h pretreatment with 100 ng/ml LPS, 20 ng/ml IFNγ, 1 µM sAβ and 1 µM fAβ. **(M)** Corresponding representative curves when stimuli is withdrawn just before the measurements. Fold change in compared to control vehicle group after **(O)** 2 h (n=4 batches) and **(P)** 6 h (n=3 batches) depicting time-dependent response in vehicle and LPS groups. Respective graphs for isogenic and *PSEN1ΔE9* iMGLs at **(Q)** 2h (n=8 batches) and **(R)** 6h (n=2 batches). **(S)** Fluorescent Aβ phagocytosis after 5h incubation in isogenic, *PSEN1ΔE9*, *APOE3* and *APOE4* experiments. **(T,U)** LPS 100 ng/ml reduces phagocytosis of fluorescent Aβ after 5h in both *PSEN1ΔE9* iMGLs and their isogenic controls. **(V)** *APPswe* iMGLs secreted less IL-6 and TNFα compared to control iMGLs after 24 h treatment with 100 ng/ml LPS, and **(W)** less IL-6 and RANTES compared to control iMGLs upon 20 ng/ml IFNγ (n=3-4 batches each with 4 wells). **(X)** *PSEN1ΔE9* iMGLs secreted less IL-6, TNFα, RANTES, and IL-8 after LPS treatment, and **(Y)** less RANTES after IFNγ treatment compared to their isogenic controls (n=4-7 batches, each with 4 wells). Data presented mean ± SEM unpaired two-tailed t-test, one-way ANOVA or two-way ANOVA followed by Bonferroni's post hoc test,*$p<0.05$, **$p<0.01$, ***$p<0.001$.

Supplemental Tables

Table S1. RPKM/FPKM values of genes of different cell types used to obtain the heatmap. Related to Figure S3. Included as a separate excel file.

Table S2. Signature of microglia genes used to perform hierarchical clustering. Related to Figure 1.

FUCA2	*SMAP2*	*TGFB1*	*ZBTB45*	*GOLM1*	*RPTOR*	*LEMD2*	*CXXC5*	*TMEM63A*
SYPL1	*ZMPSTE24*	*TMEM147*	*IRF2BPL*	*AKIRIN2*	*ZNF787*	*TAF6L*	*PIK3CD*	*TCF4*
IFFO1	*SCAMP1*	*ERF*	*SUPT7L*	*LMO2*	*RHOB*	*STX5*	*RGS19*	*PELI1*
EXTL3	*LPCAT2*	*HSPB1*	*YIPF4*	*CD63*	*SRPRB*	*FAM102B*	*BSG*	*GPAA1*
BID	*EDEM2*	*YKT6*	*ALG5*	*CD164*	*OSBPL11*	*IER5*	*STARD5*	*MAN1A2*
GLT8D1	*ERP29*	*TGFBR1*	*SLC35B1*	*GNS*	*MARCH1*	*PPP1R21*	*DCAKD*	*SLC29A3*
RNASET2	*CDIP1*	*ZFAND5*	*B4GALT4*	*EPC2*	*GTF2H2*	*TGFBR2*	*MZT2A*	*YTHDF2*
IFNΓR1	*CMTM6*	*TSPAN14*	*STAU1*	*BIN1*	*YIPF5*	*ABHD6*	*NRROS*	*PNP*
ATP6V0A1	*TMEM101*	*SYNGR2*	*SOX4*	*LRRC8A*	*SLC12A9*	*ZNF513*	*RHOG*	*SFT2D1*
MFAP3	*AGO1*	*TMEM104*	*TM9SF2*	*ST6GALNAC4*	*MFHAS1*	*DUSP7*	*FAM210A*	*UBE2J1*
AGA	*MFSD11*	*TNFAIP1*	*MBOAT7*	*DENND4C*	*TACC1*	*DAGLB*	*CD151*	*HACD2*
HSPA5	*MAST3*	*GAB1*	*FAM110A*	*CNPY3*	*MED22*	*GALNT10*	*MPI*	*ZNF580*
HEXB	*KCNK6*	*CD81*	*ERGIC3*	*FCHSD2*	*MSRB2*	*CAMLG*	*CTC1*	*SFT2D2*
HERPUD1	*RNF215*	*ELK3*	*IRF3*	*NUMA1*	*RGS10*	*PEX2*	*CALR*	*SIPA1*
GINM1	*MFNG*	*CNOT2*	*SLC10A3*	*RDX*	*PAK1*	*MID1IP1*	*ARID3B*	*DDAH2*
GDI2	*HPS4*	*LPCAT3*	*TMEM175*	*ADAM10*	*SOGA1*	*NDST2*	*ZBTB18*	*IRF9*
CASP8	*CCDC134*	*LDHB*	*YWHAH*	*ATRAID*	*PIP4K2A*	*TMEM135*	*LACC1*	*ALG3*
TMEM206	*SUN2*	*PRKAB1*	*ATF4*	*ATAD1*	*PDE3B*	*TSC22D4*	*FIZ1*	*DDX3X*
MEF2A	*PACSIN2*	*SERINC1*	*TPST2*	*ENTPD1*	*SCOC*	*MARS*	*MCFD2*	*PPP2R2A*
ERLEC1	*ALKBH1*	*SAYSD1*	*DNAJB9*	*ITGAV*	*FAM49B*	*PDIA3*	*NRIP1*	*TMEM185B*
SEL1L	*ARHGAP5*	*FBRSL1*	*SNX6*	*COPS4*	*CMTM7*	*TP53I13*	*ATP6AP2*	*TAPBP*
FAM3A	*ABHD12*	*RNF130*	*MAP1S*	*RAP1GDS1*	*SLFN13*	*NCKAP5L*	*TTC3*	*RDH14*
DERL2	*ADNP*	*ARSB*	*PPT1*	*BMP2K*	*PLCL2*	*NUDT16L1*	*PAQR7*	*GNG10*
ST6GAL1	*CTSZ*	*TTC1*	*MGAT1*	*CCNG2*	*CNOT8*	*TMUB2*	*SPATA13*	*IL10RB*
PICALM	*CST3*	*TXNDC15*	*NDFIP1*	*PAPSS1*	*MED7*	*MAT2A*	*PTTG1IP*	*TWF2*
HACD3	*RP2*	*KLHL18*	*IL13RA1*	*DUSP6*	*ST3GAL2*	*INPP5D*	*TM2D3*	*GATC*
SLC46A1	*CLN5*	*RTN4*	*STARD3*	*GIT2*	*SLC35B2*	*COMMD8*	*SNN*	*SRGAP2*
IL4R	*MGRN1*	*GGCX*	*CHSY1*	*CSAD*	*SPPL3*	*MAP2K1*	*BTBD6*	*STRADA*
ACER3	*N4BP1*	*GORASP2*	*SERPINF1*	*LPAR6*	*SKI*	*INO80E*	*ATP6V0A2*	*CYFIP1*
MKNK1	*SLC38A7*	*NFE2L2*	*PTPRA*	*RBM26*	*WASF2*	*PWWP2A*	*SP1*	*ORAI1*
REXO1	*USP10*	*TMEM59*	*SERINC3*	*TSPAN3*	*F11R*	*ZNF282*	*ZFP36L1*	
EPB41L2	*LMF1*	*SCAMP3*	*SARAF*	*SCAMP2*	*B4GALT3*	*ELP5*	*BICD2*	
STX7	*RAB11A*	*RGS2*	*CTIF*	*UNC45A*	*IFNΓR2*	*PFKFB3*	*TPCN1*	
SLC35C2	*BMF*	*ABCD3*	*VHL*	*ARMC5*	*ARHGAP27*	*KBTBD2*	*SEMA4D*	
SESN1	*LEPROTL1*	*RPS6KA1*	*ARL8B*	*PRPSAP2*	*BTG2*	*RNF139*	*PLSCR3*	
CLDND1	*ASAH1*	*CCNI*	*IL6ST*	*G6PC3*	*HK2*	*JAGN1*	*TSPYL1*	
RNF13	*CLPTM1*	*HS1BP3*	*TMED7*	*GALNT1*	*CCDC107*	*BCL2L1*	*PNRC2*	
OXCT1	*SNAPC2*	*NEK6*	*NAA35*	*SLC16A3*	*FMNL3*	*CLSTN1*	*SLC35E2B*	

Table S3. Demographic information of each iPSC-line. Related to Figure 2. See also Figure S3.

Alias	Cell line	Sex	Health status	Age at biopsy	Mutation genotype	Sample origin	Reprogramming method	Karyotype	Reference
CTRL	Ctrl1	F	Healthy	Adult	-	Skin biopsy	SeV 1.0	46XX Normal	Holmqvist et al. 2016
CTRL	Ctrl3	F	Healthy	44 y	-	Skin biopsy	SeV 1.0	46XX Normal	Oksanen et al. 2017
spPSEN	AD2	M	FAD	48 y	*PSEN1ΔE9* deletion	Skin biopsy	SeV 2.0	46XY Normal	Oksanen et al. 2017
pPSEN	AD3	F	FAD pre-symptomatic	47 y	*PSEN1ΔE9* deletion	Skin biopsy	SeV 2.0	46XX Normal	Oksanen et al. 2017
spISO	AD2 iso	M	FAD corrected	48 y	*PSEN1ΔE9* corrected	Skin biopsy	SeV 2.0 CRISPR/Cas9	46XY Normal	Oksanen et al. 2017
pISO	AD3 iso	F	FAD corrected	47 y	*PSEN1ΔE9* corrected	Skin biopsy	SeV 2.0 CRISPR/Cas9	46XX Normal	Oksanen et al. 2017
spAPP	LL008	F	FAD	48 y	*KM670/671NL* APP Swedish	Skin biopsy	SeV 1.0	46XX Normal	Oksanen et al. 2018
pAPP	LL116	F	FAD pre-symptomatic	30 y	*KM670/671NL* APP Swedish	Skin biopsy	SeV 2.0	46XX Normal	Figure S3.
APOE3	MBE 2968 clone 1	F	Healthy	65 y	*APOEε3/3*	Skin biopsy	Episomal reprogramming by nucleofection	46XX Normal	Figure S3.
APOE4	TOB 0002 clone 3	F	Non-symptomatic	52 y	*APOEε4/4*	Skin biopsy	Episomal reprogramming by nucleofection	46XX Normal	Figure S3.
APOE3	HC1	M	Healthy	57 y	*APOEε3/3*	Skin biopsy	mRNA	46XY Normal	Balez et al., 2016
APOE3	HC2	F	Healthy	75 y	*APOEε3/3*	Skin biopsy	mRNA	46XX Normal	Muñoz et al., 2018
APOE 3/4	HC3	F	Healthy	59 y	*APOEε3/4*	Skin biopsy	mRNA	46XX Normal	UOW - manuscript in preparation
APOE 3/4	LOAD1	M	LOAD	65 y	*APOEε3/4*	Skin biopsy	mRNA	46XY Normal	Balez et al., 2016
APOE4	LOAD2	F	LOAD	83 y	*APOEε4/4*	Skin biopsy	mRNA	46XX Normal	UOW - manuscript in preparation
APOE4	LOAD3	M	LOAD	77 y	*APOEε4/4*	Skin biopsy	mRNA	46XY Normal	Ooi et al., 2013

FAD, famimial Alzheimer's disease; LOAD, late-onset Alzheimer's disease; F, female; M, male; y, years.

Supplemental Experimental Procedures

Karyotyping

iPSCs were confirmed to have normal euploid karyotypes via Giemsa (G-banding) staining (pAPP) or by virtual karyotyping (TOB0002c3, MBE2968c1)(Figure S3). For Giemsa staining iPSCs were arrested with 200 ng/ml KaryoMAX® Colcemid™ (Invitrogen), harvested and 20 metaphase cells were analyzed at the Eastern Finland Laboratory Centre Joint Authority Enterprise (ISLAB, Kuopio, Finland). In virtual karyotyping the copy number variation (CNV) analysis of original fibroblasts and iPSCs was performed using HumanCore Beadchip arrays (Illumina). CNV analyses were performed using PennCNV and QuantiSNP (Wang et al., 2007, Colella et al., 2007) with default parameter settings. Chromosomal aberrations were deemed to involve at least 10 contiguous single nucleotide polymorphisms (SNPs) or a genomic region spanning at least 1MB. The B allele frequency (BAF) and the log R ratio (LRR) were extracted from GenomeStudio (Illumina) for representation. All three lines were confirmed to express high levels of pluripotent markers and to have the ability to form all three germ layers by immunocytochemistry. Embryoid bodies were obtained as described (Lim et al., 2013) and using tri-lineage differentiation kit (Stem Cell Technologies).

Flow Cytometer Analysis

The flow cytometer analysis was performed every second day throughout the 24-day differentiation process. Cells were detached with Accutase, centrifuged 300 x g, 5 min and filtered through a 70 µm mesh (Corning). Approximately 200 000 cells were used for each sample and staining controls, including unstained, single color, and secondary-only. Fluorescence minus one (FMO) controls were also prepared for gating purposes. Cells were stained with Zombie NIR fixable viability dye (1:1000, Biolegend), blocked with human FcR blocking reagent (Miltenyi Biotec), and then incubated with conjugated antibodies for 30 min at 4°C. The following antibodies were used: CD11b-APC-eFluor780 (M1/70), CD34-APC (4H11), CD41a-BB515 (HIP8), CD45-PerCP/Cy5.5 (2D1), CD117 (cKit)-BB515 (104D2), CD144 (VE-cadherin)-PE (55-7H1), CD235a (HIR2)-BB515 (GA-R2), and CD309 (KDR)-PE (89106). For intracellular staining, cells were fixed in Fix/Perm buffer for 25 min (Foxp3 Buffer Set, eBioscience), incubated with primary antibody IBA1 (1:50, Wako) for 40 min at 4°C, followed by labeling with secondary antibody goat anti-rabbit Alexa Fluor 488 (1:1000, Invitrogen) for 30 min at RT. Samples were washed between each step and resuspended in flow buffer containing 1% FBS in PBS. Samples were run on a FACSAriaIII (BD Biosciences), equipped with 488 and 633nm lasers with standard configuration or on CytoFlex S (Beckman Coulter) equipped with 405, 488, 561, and 638nm lasers. At least 50 000 single events were collected. Data was analyzed with FCSExpress v6 (De Novo) or CytExpert v2.3 (Beckman Coulter). The flow cytometry analysis was repeated with 4 cell lines including both AD and isogenic genotypes from 2-3 batches.

RNA-Seq and analysis

iMGLs were cultured at density of 2 mln cells per PDL-coated 6 cm dish and total RNA was extracted using mirVana™ miRNA Isolation Kit (Invitrogen) following manufacturer's guidelines. RNA integrity (RIN) was measured for all samples using the Bioanalyzer Agilent 2100 series. The quality was confirmed with Advanced Analytical Fragment Analyzer at Finnish Functional Genomics Centre (FFGC, Turku, Finland) and further library construction and sequencing was performed at FFGC. Total of 300 ng of high integrity RNA with RIN > 9.1 was used to generate sequencing libraries with Illumina TruSeq® Stranded mRNA to obtain poly-A mRNA. The high quality of the libraries was confirmed with Advanced Analytical Fragment Analyzer and the concentrations of the libraries were quantified with Qubit® Fluorometric Quantitation (Life Technologies). The samples were sequenced as single-end 50 bp reads on the Illumina HiSeq 3000 instrument.

Raw FASTQ files were analyzed for quality assessment using FastQC software. Read alignment and transcript quantification were performed using RSEM 1.3.1(Li, Dewey, 2011) with "--strandness reverse" and "--estimate-rspd" parameters. Hg38 was used as reference genome. All subsequent analyses were conducted with the R/Bioconductor platform. RSEM estimated counts were imported using the package Tximport (Soneson, Love & Robinson, 2015). This package allows to incorporate the average transcript length per gene as a normalization factor that can be used with statistical tools such as limma (Ritchie et al., 2015) and DESeq2 (Love, Huber & Anders, 2014). Hierarchical clustering was performed together with published data (Abud et al., 2017) using the function "hclust" with Euclidean distance on FPKM expression data. The analysis was performed using microglia signature genes (Table S2) adapted from already published data (Lavin et al., 2014) provided by the Bioconductor AUCell package (Aibar et al., 2017). Mouse identifiers have been mapped into HGNC symbols through the NCBI HomoloGene database (Wheeler et al., 2007). Genes with expression (< 1 FPKM) across all samples were discarded. Before clustering and other comparisons with data in Abud et al., the following preprocessing steps have been performed. The two studies have been separately log2-transformed (adding a pseudo-count of 1) and normalized for row using the function "normalize.quantiles" of the package preprocessCore that performs a normalization based on upon the concept of a quantile-quantile plot (Bolstad et al., 2003). Subsequently, data

have been batch corrected to remove the bias due to the technical variability of the two studies. Batch correction was performed using the function "removeBatchEffect" of the limma package.

qRT-PCR

The RNA was extracted from 10^6 *APOE* iMGLs, iPSCs and blood-derived macrophages using TRIsure reagent (Bioline) and genomic DNA was removed with TURBO DNA-free (Thermo Fisher Scientific) following the manufacturer's instructions. RNA concentration was analyzed using a Nanodrop 2000C spectrophotometer (Thermo Fisher Scientific). RNA was reverse transcribed to cDNA using the Tetro cDNA synthesis kit (Bioline) and Oligo dT18 primers incubated at 45 ^{o}C for 30 min followed by a 5 min incubation at 85 ^{o}C to terminate the reaction. Gene expression was measured by qRT-PCR using SENSIfast SYBR No-ROX PCR mix (Bioline) and a Rotor Gene 3000 Real-time PCR machine (Corbett Research) with 40 cycle amplification. Melt-curve analysis and gel electrophoresis were utilised to check amplicon size. Reactions were conducted in duplicate whilst non-template controls (substituting cDNA for water) and RNA controls were implemented to confirm that contamination, primer dimers and genomic DNA were not contributing to the signal. Data was normalised to GAPDH expression, sample efficiency/cycle threshold values were determined using LinRegPCR (Ruijter et al., 2009) and relative gene expression was determined by using the comparative threshold cycle method (Schmittgen, Livak, 2008). RNA was also extracted from *APPswe* and *PSEN1ΔE9* iMGLs and iPSCs by mirVana™ miRNA Isolation Kit (Invitrogen). Subsequent cDNA synthesis was performed with Maxima reverse transcriptase (Thermo Scientific) and the mRNA expression levels were determined by qRT-PCR (StepOne Plus Real-Time PCR system; Life Technologies) using TaqMan assay mixes (Thermo Scientific). Expression levels were normalized to *ACTB* and *GAPDG* expression.

Table of primers assay mixes used for mRNA expression studies.

Gene	**Identifier**	**Source**
ACTB	Hs99999903_m1	TaqMan
GAPDH	Hs02758991_g1	TaqMan
C1QA	Hs00706358_s1	TaqMan
C1qR	Hs00362607_m1	TaqMan
CD11b	Hs00355885_m1	TaqMan
P2RY12	Hs00224470_m1	TaqMan
CR1	Hs00559348_m1	TaqMan
CSF1R	Hs00911250_m1	TaqMan
PROS	Hs00165590_m1	TaqMan
GAS6	Hs01090305_m1	TaqMan
GPR34	Hs00271105_s1	TaqMan
MERTK	Hs01031979_m1	TaqMan
IRF8	Hs00175238_m1	TaqMan
PU.1	Hs02786711_m1	TaqMan
TREM2	Hs00219132_m1	TaqMan
TYROBP	Hs00182426_m1	TaqMan

Table of primers used for mRNA expression studies.

Target	Sequence	Species
hF_ITGAM-CD11B	GAAAGGCAAGGAAGCCGGAG	human
hR_ITGAM-CD11B	TGGATCTGTCCTTCTCTTAGCCG	human
hF_CX3CR1	TGGGGCCTTCACCATGGAT	human
hR_CX3CR1	GCCAATGGCAAAGATGACGGAG	human
hF_P2ry12	TTTGTGTGTCAAGTTACCTCCG	human
hR_P2ry12	CTGGTGGTCTTCTGGTAGCG	human
hF_IRF8	AGTAGCATGTATCCAGGACTGAT	human
hR_IRF8	CACAGCGTAACCTCGTCTTC	human
hF_MERTK	CTCTGGCGTAGAGCTATCACT	human
hR_MERTK	AGGCTGGGTTGGTGAAAA	human
hF_PROS1	TTGCACTTGTAAACCAGGTTGG	human
hR_PROS1	CAGGAACAGTGGTAACTTCCAG	human
hF_TGFBR1	ACGGCGTTACAGTGTTTCTG	human
hR_TGFBR1	GCACATACAAACGGCCTATCTC	human
hF_GAS6	CTCGTGCAGCCTATAAACCCT	human
hR_GAS6	TCCTCGTGTTCACTTTCACCG	human
hF_C1QA	TCTGCACTGTACCCGGCTA	human
hR_C1QA	CCCTGGTAAATGTGACCCTTTT	human
hF_GPR34	GCAAGGTTGTGGGAACACTGT	human
hR_GPR34	AGCGATCCAAACTGATGAATCC	human
hF_ITGB5	GGAAGTTCGGAAACAGAGGGT	human
hR_ITGB5	CTTTCGCCAGCCAAATCTTCTC	human
hF_CD14	ACTTATCGACCATGGAGCGC	human
hR_CD14	AGCTCACAAGGTTCTGGCGT	human
hF_TMEM119	CTTCCTGGATGGGATAGTGGAC	human
hR_TMEM119	GCACAGACGATGAACATCAGC	human
hF_SPI1	AGCCATAGCGACCATTAC	human
hR_SPI1	CTCCGTGAAGTTGTTCTC	human
hF_GAPDH	GAGCACAAGAGGAAGAGAGAGACCC	human
hR_GAPDH	GTTGAGCACAGGGTACTTTATTGATGGTACATG	human

Differentiation of human monocyte-derived macrophages from peripheral blood mononuclear cells

Human peripheral blood mononuclear cells (PBMCs) were isolated from the whole blood of anonymous donors (Australian Red Cross Blood Service, NSW) using Ficoll-Paque Plus (GE Healthcare) and density-gradient centrifugation. Briefly, whole blood was diluted 1:2 in phosphate buffered saline (PBS, layered above Ficoll and centrifuged for 45 min at 200 xg without deceleration. Following centrifugation, distinct phases were separated and the PBMC layer was collected and diluted 1:2 in PBS. Suspension was centrifuged at 500 x *g* for 10 min at 4°C. The pellet was washed three times with PBS by centrifugating 500 x *g* for 10 min at 4°C. Primary monocytes were isolated using magnetic microbead separation using CD14-conjugated microbeads under manufacturer specifications (Miltenyi Biotech) and positively selected cells were separated using LS+ columns (Miltenyi Biotec) positioned on a MidiMACS magnet (Miltenyi Biotec). Subsequent differentiation of CD14+ to macrophages was achieved by culturing the CD14+ cells in in high glucose DMEM, 10% FBS, 1% GlutaMAX, 1% P/S and 15 ng/ml MCSF (Miltenyi Biotec). The cells were seeded onto nunclon treated dishes at 10^6 cells/mL and incubated for 7 days at 37 ºC, 5% CO2. Differentiation was determined by observing cell morphology in a Nikon TS100 light microscope (Nikon).

3D co-cultures

3D thin-layer Matrigel cultures were prepared as previously described (Choi et al., 2014, Kim et al., 2015). iPSC-derived neurons were resuspended at $1x10^6$ cells/ml with 1:10 diluted Matrigel. plated on poly-L-ornithine-coated coverslips (Thermo Scientific) and left to polymerize overnight. On the next day, wells were filled with neural differentiation medium, consisting of DMEM/F-12 and Neurobasal (1:1), 1% B27 without vitamin A, 0.5% N2 supplement, 1% GlutaMAX™ and 0.5%P/S (all from Gibco), and the medium was changed every 3-4 days for 4-months. Then D16 iMGLs were applied on the top of cultures at density of 100,000 cells/ml. The 3D co-cultures were fixed and immunostained 7 days after incorporation of iMGLs.

3D cerebral brain organoids were generated as described (Lancaster, Knoblich, 2014). In brief, single iPSCs were seeded for embryoid body cultures in E8 with 20 µM Y-27632 on Nunclon Sphera 96-well plate. On D6, neuroinduction was initiated by replacing to 1:1 E8 and neuroinduction medium (NIM) composing of DMEM/F-12, 1% N2, 1% GlutaMAX, 1% of non-essential amino acid mixture (NEAA), 0.5% P/S (all from Gibco) and 5U/ml Heparin (LEO Pharma). On D11, the spheres were embedded into Matrigel droplets, and transferred into differentiation medium without vitamin A (Dif-A) composed of 1:1 DMEM/F-12 and Neurobasal, 1% GlutaMAX, 0.5% NEAA, 0.5% N2, 0.5% B27 without vitamin A, 0.5% P/S, 2.5 µg/ml insulin and 50 µM 2-mercaptoethanol (Sigma). On D15, the organoids were transferred to magnetic spinners (Corning) in Dif+A, which was otherwise identical to Dif-A, but B27 with vitamin A was used. For organoid and iMGLco-cultures, 200 0000 D16 iMGLs were transferred to 6-well ULA-plates with 10 organoids in Dif-A. After iMGLs freely attached to the organoids for 6 h, the organoids were transferred back to the magnetic spinners and were collected on D60 for immuhistochemical analysis.

Immunocytochemistry

The cell cultures were fixed in 4% paraformaldehyde (PFA), permeabilized in 0.5% Triton X-100 (Sigma) and 0.2% Tween20 or in 0.2% Tergitol-type NP-40 + 0.3 M glycine, and blocked with 10% normal goat serum (NGS). Primary antibodies were incubated overnight at 4°C followed by labelling with Alexa Fluor 488 (1:1000) and 568 (1:500) conjugated anti-rabbit secondary antibodies (Thermo Fisher Scientific) and nuclei were stained with 5 µg/ml Hoechst 33258 (Sigma) or 1 µg/mL Hoechst 33342 (Invitrogen). Reagents were prepared in tris-buffered saline that was used for washing between each step. 3D thin-layer Matrigel co-cultures were fixed and immunostained similarly but with longer incubation times as previously described (Kim et al., 2015, Choi et al., 2014). Coverslips were mounted on glass microscope slides using Prolong Gold Antifade reagent (Thermo Fisher Scientific) or mounting medium (Southern Biotech). Organoids were fixed with 4% PFA for 4 h followed by overnight incubation in 30% sucrose (VWR) at 4C and were then embedded into O.C.T. Compound (Sakura) for sectioning to 20 µm slices using Cryotome (Leica CM1950). Sections were transferred on microscope slides (Thermo Scientific), blocked in 10% NGS (Millipore) in 0.05% Tween20 (Sigma), incubated with a rabbit anti-Iba1 primary antibody overnight followed by secondary antibody Alexa fluor 568 goat anti-rabbit (1:500) labeling. Slides were mounted in Vectashield mounting medium with DAPI (Vector) for imaging. Staining cotrols that omitted the primary antibody or substituted it with an IgG isotype, were used to confirm staining specificity. Immunocytochemistry was visualized using a ZEISS LSM 800 Airyscan super resolution microscope (ZEISS) with 10x and 40x objectives, and 2 x GAsp and 1 x Airyscan detectors. Super resolution images were taken as z-stack images and were presented as maximum intensity projections. Images were exported using ZEN 2.3 software. Imaging conditions were kept constant across iMGLs and negative controls.

Table of primary antibodies used for immunocytochemistry.

Target	Dilution	Source	Catalog number
rabbit anti-Iba1	1:500	Wako	019-19741
rabbit anti-Iba1	1:500	Abcam	ab153696
rabbit anti-TMEM119	1:100	Abcam	ab185333
rabbit anti-CX3CR1	1:100	Abcam	ab8021
rabbit anti-TREM2	1:400	Cell Signaling Technology	91068
rabbit anti-PU.1	1:500	Cell Signaling Technology	2266
rabbit anti-P2RY12	1:125	Sigma	HPA014518

Western Blotting

Western blotting was done as described (Viswanathan et al., 2011) with minor changes. Two million iMGLs were lysed into T-PER tissue extraction buffer with a Halt™protease inhibitor and Halt™phosphatase inhibitor cocktails (all from Thermo Fisher Scientific). Protein concentrations were determined using Pierce™ BCA Protein Assay Kit (Thermo Fischer Scientific) and 15 µg proteins were separated on NuPAGE™ 4–12% Bis-Tris Midi gels (Invitrogen) under reducing conditions and blotted onto polyvinylidene difluoride membranes. The iBlot 2 PBDF Regular Stacks and Dry Blotting System (both from Invitrogen) were used to transfer the proteins. The membranes were probed with the anti-APP (1:2000, Sigma) and anti-PSEN1 (1:1000, Chemicon) to detect FL- and CTF-PSEN, and anti-GAPDH (1:15000, Abcam) antibodies and labeled with horseradish peroxidase (HRP)-conjugated mouse and rabbit secondary antibodies (GE Healthcare). Proteins were detected and visualized by using enhanced chemiluminescence substrate prime (GE Healthcare) and BioRad Chemi Doc™ imaging system. Images were quantified using Image Lab (Bio-Rad Laboratories, Inc.) and protein levels were normalized to GAPDH.

Aβ ELISA
The amounts of Aβ1-40 and Aβ1-42 were measured from 48 h conditioned cell culture medium and cell extract with Amyloid beta 40 and 42 Human ELISA Kits (Invitrogen). The cells were seeded on D16 on PDL-coated 24-well Nunc plates at final concentration of 250 000 cells/well and maintained normally until D24 before collecting the samples. Protease inhibitor cocktail (Sigma) with a serine protease inhibitor, was added 1:200 to samples. Conditioned medium from iPSC-derived neurons was used as positive control and the sample was prepared as described previously (Oksanen et al., 2017).

Ca^{2+} Imaging
iMGLs on PDL-coated coverslips were loaded with the calcium-sensitive fluorescent dye Fluo-4, AM (5 µM, Invitrogen) for 30 min followed by a 10-min washout in the basic solution containing 2.5 KCl (Scharlau Chemicals), 152 NaCl, 1 MgCl2, 10 HEPES (all from VWR chemicals), 10 glucose (MP Biomedicals) and 2 CaCl2 (Merck KGaA) at pH 7.4 (all mM). Fluorescence was visualized using the imaging setup (TILL Photonics GmbH) consisting of a monochromatic light source and a CCD camera (SensiCam) with ex 495 nm, em ≥520 nm, exposure time 100 ms and binning 2. The baseline was measured for 2 min before applying either 100 µM ATP or ADP (both Sigma) for 5 s, followed with 2 min stabilization, and application of 10 µM ionomycin (Tocris Bioscience) for 2s to induce maximal response. The chemicals were applied using a fast perfusion system Rapid Solution Changer RSC-200 (BioLogic Science). For quantification, the baseline was subtracted and the maximum amplitudes evoked by ATP or ADP were divided by the maximum amplitude of ionomycin to get a ratio. Data were analyzed using FEI offline analysis (TILL Photonics) and ImageJ (U. S. National Institutes of Health) and further analysis was automatized using MatLab (The MathWorks, Inc) and Origin (OriginLab Corporation).

Migration assay
IncuCyte® scratch wound cell migration assay (Sartorius) was performed according to manufacturer's instructions through real-time visualization. In brief, confluent monolayer of iMGLs on PDL-coated 96-well ImageLock™ microplates (EssenBioScience) was wounded using a 96-well WoundMaker to create homogeneous, 700-800µm wide wounds and the cells were treated with 100 µM ATP, ADP, or CX3CL1 (Peprotech), or freshly reconstituted 1 µM sAβ (Bachem). Live-cell imaging scans in bright field were repeated every hour for 24 h. The wound width, confluence and relative wound density were analyzed with IncuCyte S3 2018 software (Essen BioScience).

Phagocytosis assays
pHrodo™ Zymosan A BioParticle phagocytosis assay (Thermo Fisher Scientific) was performed using IncuCyte live cell imaging. iMGLs were prestimulated for 24 h with 100 ng/ml LPS (Sigma), 20 ng/ml IFNγ (Peprotech) or LPS-IFNγ (100ng/ml, 20 ng/ml) or were treated with 1µM sAβ or insoluble fAβ Aβ1-42 at the time of bead application in microglial maturation medium without FBS on PDL-coated nunc 96-well plates. fAβ was prepared from sAβ by incubating at 37°C for 7 days. pHrodo bioparticles were added in Opti-MEM (Gibco) at 62.5µg/ml and cells live-cell imaged in IncuCyte S3 every 30 minutes for 6 h to obtain fluorescent-time curve. Additionally, nuclei were stained after 2 h bead incubation with 5 µg/ml H33342 for 5 min and iMGLs were live-imaged using a ZEISS IX70 fluorescent microscope with Axio Observer.Z1 (ZEISS) with 20X magnification. The total pHrodo fluorescence intensity was normalized to cell confluence analyzed by IncuCyte S3 2018 or to number of nuclei analyzed by ImageJ. In addition, FITC Zymosan A S. cerevisiae BioParticles (Thermo Fisher Scientific) were opsonized in FBS and added on iMGLs on Matrigel-coated glass coverslips at density of 1.5 bioparticles per cell. The assay was terminated by 4% PFA fixation after 2.5-3 h. Coverslips were washed 8x for 5 min using TBS to remove free beads that had not been internalized. Nuclei were stained using 1 µg/mL Hoechst 33342 (Thermo Fisher Scientific). Coverslips were mounted on glass microscope slides using Prolong Gold Antifade reagent (Thermo Fisher Scientific) and were imaged using a Leica SP8 confocal microscope (Leica). For quantification, fluorescence was measured as corrected mean grey value and analyzed using ImageJ.

Cytometric Bead Array
Cytokine secretion iMGLs was analyzed using the Cytometric Bead Array (CBA) with human soluble protein flex sets (all from BD Biosciences). The medium was collected from plates prestimulated for 24h for pHrodo assays. Media was diluted 1:1 for LPS-treated and 1:10 for LPS-IFNγ-treated samples in assay diluent. Twenty microliters of sample or cytokine standard was incubated with 20 µl of bead mixture (bead dilutions 1:75) and then with 20ul of diluted detection reagent (1:75). Samples run on Cytoflex S (Beckman Coulter) by detecting at least 300 events for each cytokine. Beads positions clustered with channels 638/660 nm (APC) and 638/780 nm (APC-A750) off the 638 nm red laser. Cytokine reporter PE fluorescence was measured through 561/585 nm channel off 561 nm yellow-green laser. The data was analyzed with FCAP array (SoftFlow) and regression analysis was used to calculate cytokine concentrations from known standards.

MitoStress mitochondrial metabolism assay

Mitochondrial metabolism of iMGLs was analyzed with MitoStress test (Agilent) following manufacturer's guidelines. The cells were pre-stimulated for 24 h with LPS, IL-4 (Peprotech), IFNγ or with LPS-IFNγ (20 ng/ml for all) at density of 150 000 cells/well. The XF assay medium (Agilent) was supplemented with 25 mM GlutaMAX and 1 mM sodium pyruvate (Gibco). Mitochondrial electron transport chain modulators all 1 µM were injected during the assay sequentially: 1) oligomycin to inhibit ATP synthase, 2) carbonyl cyanide-4-(trifluoromethoxy)phenylhydrazone (FCCP) to disrupt the proton gradient and membrane potential, and 3) a mixture of rotenone and antimycin A (RA) to switch off the mitochondrial respiration (all from Sigma). Changes in OCR in response to injections were detected with Seahorse XF24 analyzer (Agilent). Results were normalized to total protein content measured with Pierce BCA protein assay kit and the data was analyzed with Wave 2.4 (Agilent). Mitochondrial parameters were calculated from OCRs according to manufacturer's instructions.

Experimental Procedures References

Aibar, S., Gonzalez-Blas, C.B., Moerman, T., Huynh-Thu, V.A., Imrichova, H., Hulselmans, G., Rambow, F., Marine, J.C., Geurts, P., Aerts, J., et al 2017, "SCENIC: single-cell regulatory network inference and clustering", *Nature methods*, vol. 14, no. 11, pp. 1083-1086.

Bolstad, B.M., Irizarry, R.A., Astrand, M. & Speed, T.P. 2003, "A comparison of normalization methods for high density oligonucleotide array data based on variance and bias", *Bioinformatics (Oxford, England)*, vol. 19, no. 2, pp. 185-193.

Choi, S.H., Kim, Y.H., Hebisch, M., Sliwinski, C., Lee, S., D'Avanzo, C., Chen, H., Hooli, B., Asselin, C., Muffat, J., et al 2014, "A three-dimensional human neural cell culture model of Alzheimer's disease", *Nature*, vol. 515, no. 7526, pp. 274-278.

Colella, S., Yau, C., Taylor, J.M., Mirza, G., Butler, H., Clouston, P., Bassett, A.S., Seller, A., Holmes, C.C. & Ragoussis, J. 2007, "QuantiSNP: an Objective Bayes Hidden-Markov Model to detect and accurately map copy number variation using SNP genotyping data", *Nucleic acids research*, vol. 35, no. 6, pp. 2013-2025.

Kim, Y.H., Choi, S.H., D'Avanzo, C., Hebisch, M., Sliwinski, C., Bylykbashi, E., Washicosky, K.J., Klee, J.B., Brustle, O., Tanzi, R.E., et al 2015, "A 3D human neural cell culture system for modeling Alzheimer's disease", *Nature protocols*, vol. 10, no. 7, pp. 985-1006.

Lancaster, M.A. & Knoblich, J.A. 2014, "Generation of cerebral organoids from human pluripotent stem cells", *Nature protocols*, vol. 9, no. 10, pp. 2329-2340.

Li, B. & Dewey, C.N. 2011, "RSEM: accurate transcript quantification from RNA-Seq data with or without a reference genome", *BMC bioinformatics*, vol. 12, pp. 323-2105-12-323.

Lim, S.Y., Sivakumaran, P., Crombie, D.E., Dusting, G.J., Pebay, A. & Dilley, R.J. 2013, "Trichostatin A enhances differentiation of human induced pluripotent stem cells to cardiogenic cells for cardiac tissue engineering", *Stem cells translational medicine*, vol. 2, no. 9, pp. 715-725.

Love, M.I., Huber, W. & Anders, S. 2014, "Moderated estimation of fold change and dispersion for RNA-seq data with DESeq2", *Genome biology*, vol. 15, no. 12, pp. 550-014-0550-8.

Ritchie, M.E., Phipson, B., Wu, D., Hu, Y., Law, C.W., Shi, W. & Smyth, G.K. 2015, "limma powers differential expression analyses for RNA-sequencing and microarray studies", *Nucleic acids research*, vol. 43, no. 7, pp. e47.

Ruijter, J.M., Ramakers, C., Hoogaars, W.M., Karlen, Y., Bakker, O., van den Hoff, M.J. & Moorman, A.F. 2009, "Amplification efficiency: linking baseline and bias in the analysis of quantitative PCR data", *Nucleic acids research*, vol. 37, no. 6, pp. e45.

Schmittgen, T.D. & Livak, K.J. 2008, "Analyzing real-time PCR data by the comparative C(T) method", *Nature protocols*, vol. 3, no. 6, pp. 1101-1108.

Soneson, C., Love, M.I. & Robinson, M.D. 2015, "Differential analyses for RNA-seq: transcript-level estimates improve gene-level inferences", *F1000Research*, vol. 4, pp. 1521.

Viswanathan, J., Haapasalo, A., Bottcher, C., Miettinen, R., Kurkinen, K.M., Lu, A., Thomas, A., Maynard, C.J., Romano, D., Hyman, B.T., et al 2011, "Alzheimer's disease-associated ubiquilin-1 regulates presenilin-1 accumulation and aggresome formation", *Traffic (Copenhagen, Denmark)*, vol. 12, no. 3, pp. 330-348.

Wang, K., Li, M., Hadley, D., Liu, R., Glessner, J., Grant, S.F., Hakonarson, H. & Bucan, M. 2007, "PennCNV: an integrated hidden Markov model designed for high-resolution copy number variation detection in whole-genome SNP genotyping data", *Genome research*, vol. 17, no. 11, pp. 1665-1674.

Wheeler, D.L., Barrett, T., Benson, D.A., Bryant, S.H., Canese, K., Chetvernin, V., Church, D.M., DiCuccio, M., Edgar, R., Federhen, S., et al 2007, "Database resources of the National Center for Biotechnology Information", *Nucleic acids research*, vol. 35, no. Database issue, pp. D5-12.